Controlling the Pre-Curvature of Surface Electrochemical Actuators for Microscopic Robots

2021 CNF REU Intern: Zhangqi Zheng

Intern Affiliation: Engineering Physics (intended), Cornell University

CNF REU Principal Investigator: Paul L. McEuen, Department of Physics, Cornell University

CNF REU Mentors: Samantha Norris, Department of Physics, Cornell University; Michael F. Reynolds, Department of Physics, Cornell University

Primary Source of Research Funding: 2021 Cornell NanoScale Science & Technology Facility Research Experiences for Undergraduates (CNF REU) Program via National Science Foundation under Grant No. NNCI-2025233

Contact: zz365@cornell.edu, plm23@cornell.edu, sn588@cornell.edu, mfr74@cornell.edu

Primary CNF Tools Used: ABM contact aligner, Arradiance ALD Gemstar-6, AJA sputter deposition (1&2), AJA ion mill, Heidelberg mask writer - DWL2000, Oxford 80 etchers, Xactic xenon difluoride etcher

Abstract:

Smart microscopic robots, capable of performing complicated tasks while at a few hundred microns in size, have revolutionary potential in many fields. Recent research in our group has developed a promising approach towards producing such smart microscopic robots [1]. One important component of this kind of robot is the Surface Electrochemical Actuators (SEAs) [1,2], which function as the legs of the robots. With the current recipe, the SEAs have an innate pre-curvature, causing the legs to bend underneath the bodies of the robots right after release, while ideally, we would like to control the angle of this bending. In this research, we were able to change the pre-curvatures by varying the deposition pressure of titanium during the fabrication of the SEAs, showing that we can tune the pre-curvatures of the legs of smart microscopic robots through the fabrication process.

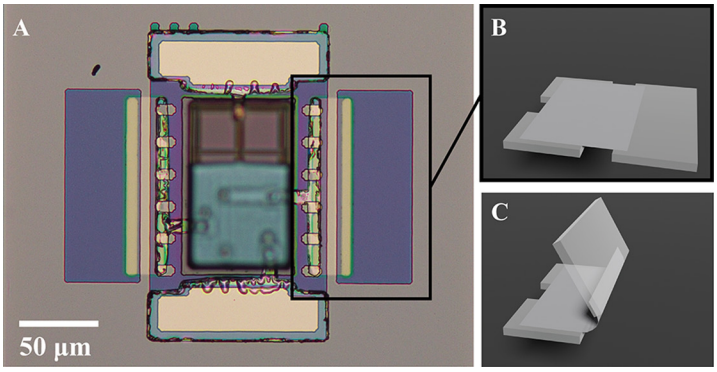

Figure 1, above: (A) Image of a smart microscopic robot before release. (B) 3D illustration of a leg of the microscopic robot before release. (C) 3D illustration of a leg of the microscopic robot after release. Figure 2, right: Fabrication process (A) metal layer, (B) polymer panel, (C) aluminum release layer, (D) after XeF_2 etching, and (E) after release.

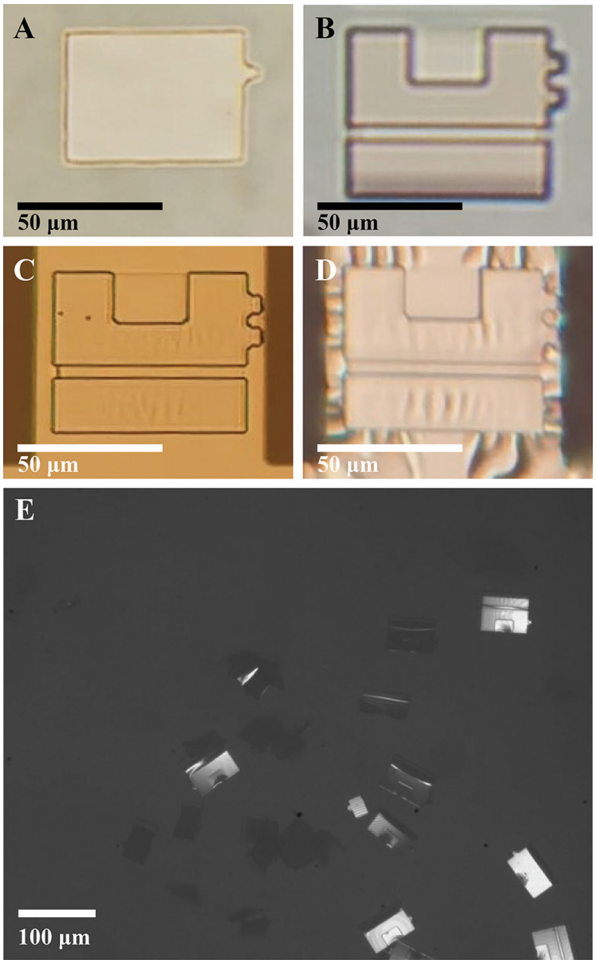

Summary of Research:

These microscopic robots developed by our group are the first of their kind, integrated with on-board circuitry that controls the motions of the robot, photovoltaics that provide power for the robot, and legs that make the robots move. Figure 1A shows an image of one of these robots when it is fully fabricated, prior to release (Reynolds, M.F. et al. Unpublished). Inside the box on the right side of the image is one of its legs, which is also shown with a 3D illustration in Figure 1B. The key component of such leg that provides its functionality is the Surface Electrochemical Actuator (SEA). Made of a 7 nm thick platinum (Pt) thin film capped on one side with about 3 nm thick of titanium (Ti), the SEAs actuate under

a voltage supply [1]. Before any actuation, however, the SEAs naturally bend towards the Pt side of the film when they are released, as shown in Figure 1C. This pre-curvature is caused by the stress of the metal films, which is largely influenced by the deposition pressure of the Ti. We use the AJA sputter deposition #2 at the CNF for depositing the Ti. Previous data collected by the CNF staff show that the pre-stress of an over 200 nm thick Ti film deposited at 3 mTorr is -178 MPa, while that of the same thickness deposited at 7 mTorr is 28 MPa. Through this research, we investigated how this difference in pre-stress due to different Ti deposition pressure causes variation in the pre-curvature of the SEAs. By fabricating SEAs with various Ti deposition pressure and measuring and comparing the pre-curvature of them, we confirmed that we can tune the pre-curvature of SEAs by changing Ti deposition pressure.

Figure 2 demonstrates the fabrication process for the leg hinges that are used for testing the pre-curvature of the SEAs. We start by depositing the Pt and Ti metal films and etching them to a rectangular shape (Figure 2A). For the purpose of this research, we deposited Ti at three different deposition pressures — 3 mTorr, 5 mTorr, and 7 mTorr — on three different silicon (Si) chips. After depositing the metal film, we fabricate the polymer panels that keeps the rest of the SEAs film in these leg hinges straight, ensuring that only the exposed SEAs film in the 3 μm gap between the panels bend when actuated (Figure 2B). We then sputter a layer of aluminum covering the hinges (Figure 2C). After we etch the Si substrate underneath, the hinges are tethered only by the aluminum (Al) on top of them (Figure 2D). For the last step we release the hinges by putting the chips upside down in Al etchant, and the chips fell off of the substrates to the bottom of the Petri® dish (Figure 2E).

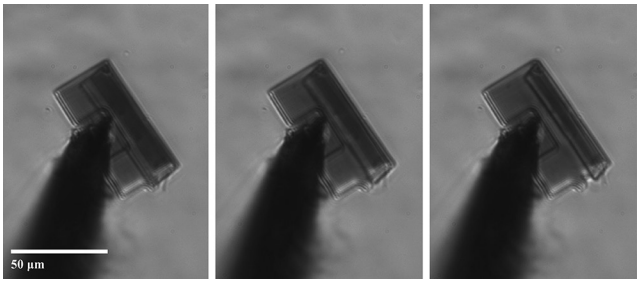

Figure 3: Optical images of a leg hinge during actuation.

We then tested the hinges for actuation by touching down to the SEAs with a Pt/Ir probe and applying a voltage through the probe. We observed actuation of hinges with Ti deposited at all three deposition pressures when we applied a triangular wave with 1.2 V amplitude (Figure 3), showing that the hinges can function as expected with the different deposition pressures.

Figure 4 shows a plot of the pre-curvatures measured from the leg hinges against the Ti deposition pressure of the hinges. Above each Ti deposition pressure is an image of a hinge fabricated with the deposition pressure. The average pre-curvature for each deposition pressure has a clear trend

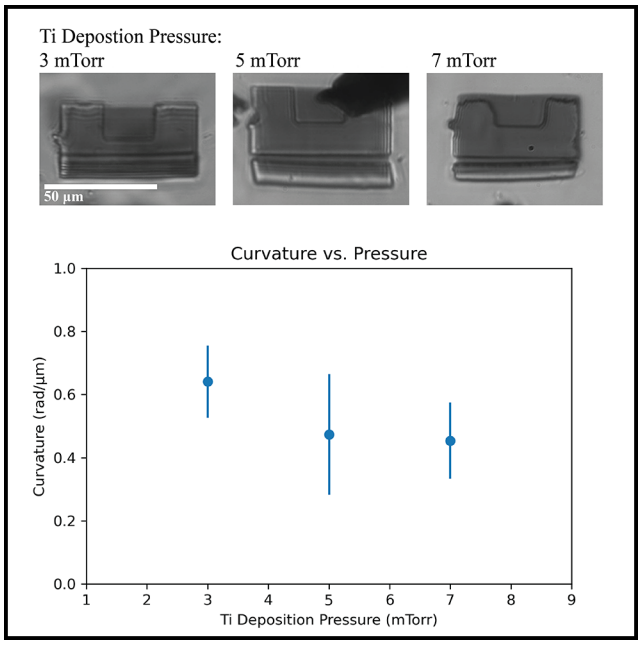

Figure 4: Data of pre-curvatures of SEAs hinges at different Ti deposition pressures.

where lower deposition pressure produces a larger pre-curvature, which matches the behavior of the pre-stresses measured at 3 mTorr and 7 mTorr. This indicates that we can tune the pre-curvature of the SEAs by changing Ti deposition pressures, and that the hinges fabricated with Ti deposited at all three deposition pressures function as expected.

Conclusions and Future Steps:

Overall, the tunability of the pre-curvature of the SEAs via changing Ti deposition pressure demonstrated in this research allows us to have better control of the initial leg shapes for smart microscopic robots. Instead of having a fixed arbitrary bending after release, this tunability allows us to fabricate future generations of smart microscopic robots with their legs bent at the angle we prefer upon release.

Acknowledgements:

I would like to acknowledge the support of the National Science Foundation, National Nanotechnology Coordinated Infrastructure, and Cornell NanoScale Facility Research Experiences for Undergraduates (CNF REU) Program (NSF grant no. NNCI-2025233). I give special thanks to my PI Dr. Paul McEuen, mentors Samantha Norris and Michael F. Reynolds, and the staff at the CNF.

References:

[1] Miskin, M. Z., et al. Electronically integrated, mass-manufactured, microscopic robots. Nature 584, 557-561 (2020).

[2] Liu, Q., et al. Micrometer-sized electrically programmable shape-memory actuators for low-power microrobotics. Science Robotics 6, (2021).

Current-Induced Magnetization Switching in a Ferrimagnetic Layer

CNF Project Number: 111-80

Principal Investigator(s): Robert A. Buhrman, Daniel C. Ralph

User(s): Qianbiao Liu, Lijun Zhu

Affiliation(s): School of Applied and Engineering Physics, Cornell University

Primary Source(s) of Research Funding: Office of Naval Research

Contact: dcr14@cornell.edu, QL63@cornell.edu

Primary CNF Tools Used: 5x stepper, AJA sputter deposition, DISCO dicing saw

Abstract:

Ferrimagnets with strong perpendicular magnetic anisotropy are interesting for their exotic spin-orbitronic effects and technological potential in high-performance magnetic storage and computing. Here we demonstrate efficient switching of ferrimagnetic layers by in-plane charge current. This result indicates the presence of a strong current-induced spin orbit torque.

Summary of Research:

Using ultraviolet photolithography (5X stepper with resist S1813) and ion milling, we patterned sputter-deposited ferrimagnetic FeTb single layers into Hall bar devices ($5\times60\ \mu m^2$) at the Cornell NanoScale Science &Technology Facility. We then fabricated electrical contacts of Hall bars by ultraviolet photolithography (5X stepper with resist S1813), AJA sputter deposition of 5 nm Ti and 150 nm Pt, and lift-off in acetone. Finally, we diced the samples into chips using the dicing saw with a silicon only blade.

As we show in Figure 1, the FeTb single layers can be switched sharply at a low current density of 8×10^6 A/cm^2. During the measurement, we applied a bias magnetic field of -3 kOe along the current direction. This finding indicates that the in-plane current induces a strong spin orbit torque in the ferrimagnetic layers.

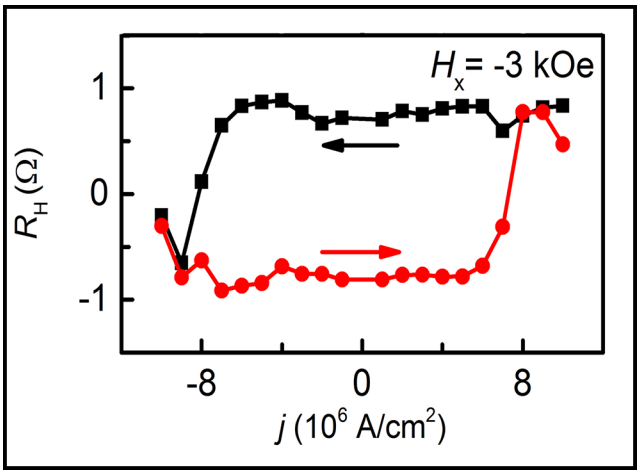

Figure 1: Anomalous Hall resistance of a ferrimagnetic FeTb thin film plotted as a function of the in-plane current density. An in-plane bias field of -3 kOe was applied along the current direction.

Separation of Artifacts from Spin-Torque Ferromagnetic Resonance Measurements of Spin-Orbit Torque for the Low-Symmetry Semi-Metal $ZrTe_3$

CNF Project Number: 598-96

Principal Investigator(s): Daniel C. Ralph

User name(s): Thow Min Jerald Cham

Affiliation(s): Laboratory of Atomic and Solid State Physics, Cornell University

Primary Source(s) of Research Funding: National Science Foundation/Division of Materials Research, Agency for Science Technology and Research (Singapore)

Contact: dcr14@cornell.edu, tc676@cornell.edu

Primary CNF Tools Used: Zeiss Supra SEM, Nabity Nanometer pattern generator, AJA sputter deposition, CVC SC4500 even-hour evaporator

Abstract:

We report measurements of spin-orbit torque generated by exfoliated layers of the low-symmetry semi-metal zirconium tritelluride ($ZrTe_3$), using the spin-torque ferromagnetic resonance (ST-FMR) technique. When the $ZrTe_3$ has a thickness greater than about 10 nm, artifacts due to spin pumping and/or resonant heating cause the standard ST-FMR analysis to give inaccurate values, indicating incorrectly that the spin-orbit torque depends strongly on the $ZrTe_3$ layer thickness. Artifact-free measurements can still be achieved over a substantial thickness range by the method developed recently to detect ST-FMR signals in the Hall geometry as well as the longitudinal geometry. For $ZrTe_3$/Permalloy samples, we measure a conventional in-plane antidamping spin torque ratio $\xi_{\parallel}^{DL} = 0.015 \pm 0.003$, and an unconventional in-plane field-like torque ratio $\xi_{\parallel}^{FL} = 0.003 \pm 0.001$. The out-of-plane antidamping torque is negligible.

Summary of Research:

We illustrate, using $ZrTe_3$/Permalloy bilayers, that extra care is required when employing the spin-torque ferromagnetic resonance (ST-FMR) technique in devices with thicker spin-orbit layers, because the magnitude of artifacts due to spin pumping and resonant heating grow relative to the spin-orbit-torque signals as a function of increasing layer thickness. One signature of such artifacts is an apparent dependence of the spin-torque efficiency on the spin-orbit layer thickness for layers much thicker than a typical spin diffusion length. We demonstrate that a recently-introduced modification of the ST-FMR technique [1], in which the ST-FMR signals are measured in the Hall geometry [2,3] as well as the usual longitudinal geometry, allows more-accurate measurements of the spin-orbit torques, separated from artifacts due to spin pumping and resonant heating. The device geometries for the measurements are shown in Figure 1.

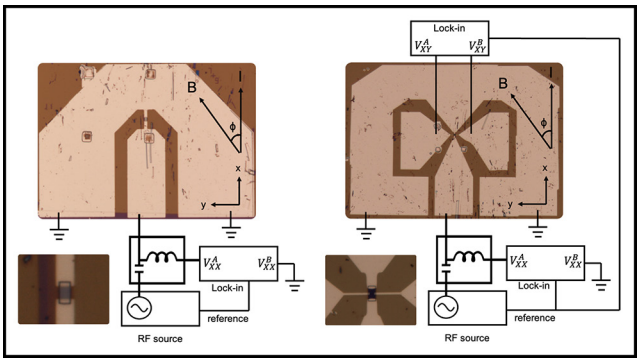

Figure 1: Schematic of a) conventional ST-FMR and b) Hall ST-FMR experimental set-ups. An additional lock-in amplifier connected across the hall leads of the device is used to read out the mixing voltage due to the change in PHE and AHE resistances.

The results of this (incorrect) standard analysis, which neglects artifact effects, are shown in Figure 2 as a function of the thickness of the $ZrTe_3$ layer. For the thinnest $ZrTe_3$ layers, the standard in-plane antidamping torque efficiency $\xi_{\parallel}^{DL}$ is weakly positive, with a value $\xi_{\parallel}^{DL} = 0.015 \pm 0.002$ for the 3 nm $ZrTe_3$ layer, but as a function of increasing $ZrTe_3$ thickness it becomes negative, with strong thickness dependence through 100 nm. At the largest $ZrTe_3$ thicknesses, the apparent magnitude of $\xi_{\parallel}^{DL}$ appears to become extremely large $|\xi_{\parallel}^{DL}| > 0.4$, even larger than the value for pure W.

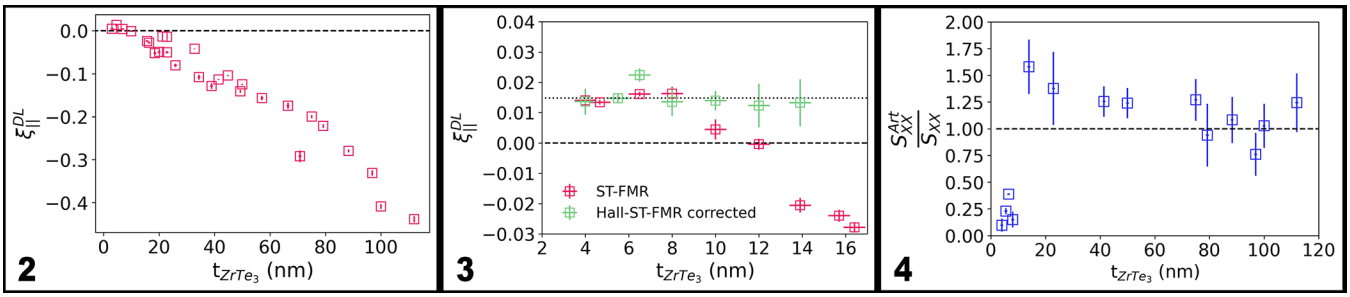

Figure 2, left: Thickness dependence of the apparent in-plane antidamping spin torque efficiency based on the incorrect standard analysis that neglects artifact from spin pumping and resonant heating. Figure 3, middle: Artifact corrected efficiency from Hall-ST-FMR for $t_{ZrTe3} < 15$ nm, showing negligible thickness dependence and absence of a sign change as $t_{ZrTe3} > 10$ nm. Figure 4, right: Ratio between V_{art} and V_S for $t_{ZrTe3} > 15$nm. V_{Art} was on the same order of magnitude as V_S, indicating that the apparent large antidamping torque signal observed for thicker flakes is likely spin-pumping dominated.

Properly accounting for spin pumping artefacts using the Hall-ST-FMR technique, we obtain the artefact corrected efficiency $\xi_{\parallel}^{DL} = 0.015 \pm 0.003$ as shown by the dotted line in Figure 3, largely independent of device thickness for $t_{ZrTe} < 15$ nm. Beyond $ZrTe_3$ thicknesses of 15 nm, the artifact voltages are too large to make an accurate determination of the spin-orbit torque, but it is clear that the apparent thickness dependence of this efficiency in the range $t_{ZrTe} > 15$ nm is due entirely to the effects of the artifact voltages, as shown in Figure 4. The non-conventional torques also remain largely independent of thickness, with values that agree with the conventional STFMR analysis.

Conclusion and Future Steps:

In summary, we have used ST-FMR to investigate the spin-orbit torques generated by exfoliated flakes of the low-symmetry semi-metal $ZrTe_3$ for a wide range of layer thicknesses in $ZrTe_3$/Py(6 nm) devices. We find that the "standard" ST-FMR analysis, which neglects the effects of artifacts due to spin pumping and resonant heating, gives incorrect values of the in-plane anti-damping torque efficiency $\xi_{\parallel}^{DL}$ for $ZrTe_3$ layers thicker than 15 nm. For the thickest layers, this incorrect standard analysis can overestimate the magnitude of $\xi_{\parallel}^{DL}$ by more than an order of magnitude, and it indicates an unphysical strong dependence of the torque efficiency on layer thickness.

ST-FMR measurements in the Hall geometry demonstrate that this strong apparent thickness dependence is due entirely to artifacts from spin pumping and/or resonant heating, not a true dependence of the spin-orbit torque on layer thickness. For $ZrTe_3$, the Hall ST-FMR measurements yield torque efficiencies $\xi_{\parallel}^{DL} = 0.015 \pm 0.003$ for the conventional in-plane antidamping torque and $\xi_{\parallel}^{FL} = 0.003 \pm 0.001$ for the unconventional in-plane field-like torque.

We suggest that ST-FMR measurements in the Hall geometry should be used as a standard technique to allow a clear separation of spin pumping and resonant heating artifacts from true spin-orbit-torque signals.

References:

[1] Saba Karimeddiny, Joseph A. Mittelstaedt, Robert A. Buhrman, and Daniel C. Ralph. Transverse and longitudinal spin-torque ferromagnetic resonance for improved mea.surement of spin-orbit torque. Phys. Rev. Applied, 14:024024, Aug 2020.

[2] Arnab Bose, Sutapa Dutta, Swapnil Bhuktare, Hanuman Singh, and Ashwin A. Tula.purkar. Sensitive measurement of spin-orbit torque driven ferromagnetic resonance detected by planar Hall geometry. Applied Physics Letters, 111(16), 2017.

[3] A. Kumar, S. Akansel, H. Stopfel, M. Fazlali, J. Akerman, R. Brucas, and P. Svedlindh. Spin transfer torque ferromagnetic resonance induced spin pumping in the Fe/Pd bi-layer system. Physical Review B, 95(6):6-12, 2017.

Anisotropic Magnetoresistance in Graphene/ Insulating Ferromagnet van der Waals Heterostructures

CNF Project Number: 598-96

Principal Investigator(s): Daniel C. Ralph

User(s): Bozo Vareskic

Affiliation(s): Laboratory for Atomic and Solid State Physics, Cornell University

Primary Source(s) of Research Funding: Air Force Office of Scientific Research

Contact: dcr14@cornell.edu, bv227@cornell.edu

Primary CNF Tools Used: Veeco Icon AFM, CVC SC4500 even/odd-hour evaporator

Abstract:

Insulating van der Waals magnets are a promising platform for spintronic applications [1]. The insulating nature of these magnets eliminates current shunting observed in spin-torque bilayer devices with metallic magnets which would lead to more efficient spin-torque devices. Furthermore, the atomically clean interfaces of van der Waal heterostructures provide a novel system to study the nature of spin transparency at the interface of two dimensional materials. However, electrical readout of the magnetic state is challenging because insulating magnets do not exhibit anisotropic magnetoresistance (AMR). Previous studies have used tunneling magnetoresistance as a readout mechanism [2,3], but these methods are difficult to incorporate into a bilayer spin-torque device. In order to achieve electrical sensitivity to the magnetic orientation, we fabricate a heterostructure of graphene and insulating ferromagnet chromium tribromide ($CrBr_3$). Low temperature magneto-transport measurements reveal an angular dependence that is consistent with an AMR mechanism, suggesting that the graphene is magnetized by proximity to $CrBr_3$.

Summary of Research:

Flakes of graphene, $CrBr_3$, and hexagonal-boron nitride (h-BN) are mechanically exfoliated on a SiO_2/Si wafer with oxide thickness of 285 nm in an inert glove box environment. Monolayer graphene flakes and few layer $CrBr_3$ are identified by optical contrast. Thickness calibration is performed by a combination of atomic force microscopy (Atomic Force Microscope – Veeco Icon) and Raman spectroscopy. In order to avoid exposure to ambient oxygen and water, $CrBr_3$ flakes were always encapsulated by h-BN prior to removal from the glove box.

The heterostructure is assembled by a dry transfer technique [4] in the glove box. h-BN is initially picked up, followed by $CrBr_3$, and lastly, graphene. Figure 1 shows a schematic of the device. The h-BN and graphene encapsulate the $CrBr_3$ from above and below, respectively. The heterostructure is then dropped onto a set of prepatterned Hall electrodes (Figure 2). Metal was deposited using the CVC SC4500 even/odd-hour evaporator.

DC transport measurements were performed in a liquid helium fridge at 5 K, which is well below the Curie temperature (~34 K) of $CrBr_3$ [5]. An in-plane field of 0.9 T was applied, and the resistance was measured as the applied field angle was swept in the plane. The AMR is defined in the bottom of Figure 3. The angular dependence of the resistance is depicted in Figure 4 and fitted to the equation at the top of Figure 3. R_0, ΔR, and ϕ_0 are treated as free parameters.

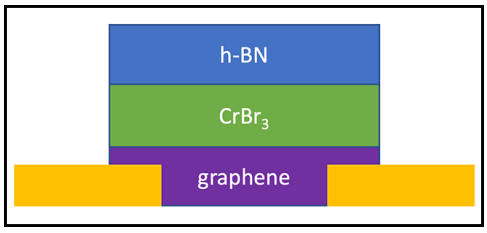

Figure 1: Schematic of monolayer graphene/chromium tribromide ($CrBr_3$) heterostructure. Insulating hexagonal boron nitride (h-BN) and graphene are used for top and bottom encapsulation, respectively, to prevent degradation of air sensitive $CrBr_3$.

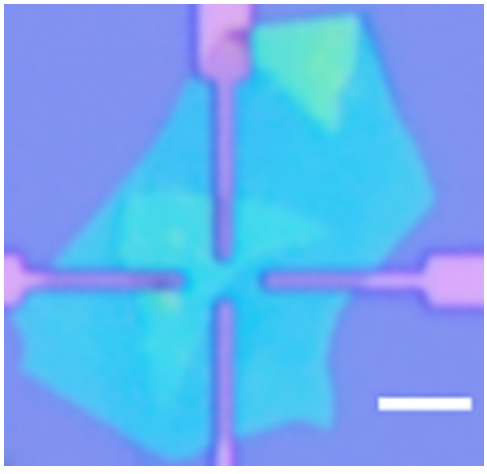

Figure 2: Micrograph of graphene/$CrBr_3$ heterostructure. Scale bar: 5 μm.

$$R = R_0 + \Delta R \cos(2(\phi - \phi_0))$$

$$\text{AMR} = \frac{R(\phi) - R(\phi = \phi_0)}{R(\phi = \phi_0)}$$

Figure 3: Above: fitting equation used to describe the angular dependence of the magnetoresistance subject to an in plane magnetic field. ϕ is the in-plane angle of the applied magnetic field, and $\phi = \phi_0$ corresponds to angle at which the current the current is parallel to the field. Below: definition of the anisotropic magnetoresistance.

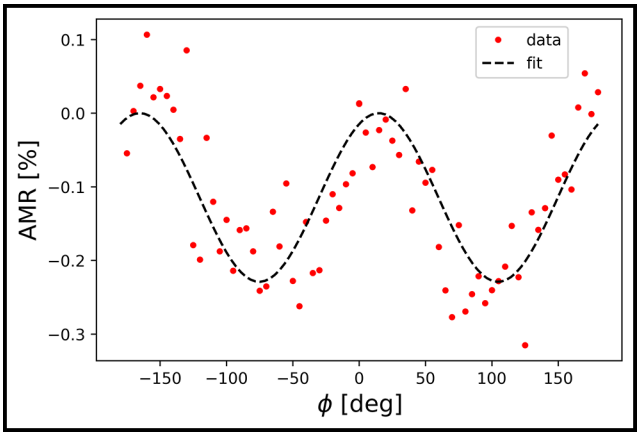

Figure 4: AMR of graphene/$CrBr_3$ heterostructure as a function of in-plane magnetic field angle. An in-plane field of B = 0.9 T was swept while applying a 1 μA current. Measurements were performed at T = 5 K. The fit is described by the top equation of Figure 3.

The periodicity of the AMR is consistent with that of conducting ferromagnetic systems described by the equation at the top of Figure 3. This suggests that the graphene is magnetized by the proximity effect. It is unlikely that the angular dependence of the magnetoresistance is due to spin Hall magnetoresistance since the spin-orbit coupling in graphene is relatively weak and graphene does not exhibit a spin Hall effect. Nonetheless, we can not rule out the possibility that spin-orbit coupling is induced in addition to ferromagnetism in graphene by the proximity effect.

References:

[1] Mak, K. F., Shan, J., and Ralph, D. C.; Probing and controlling magnetic states in 2D layered magnetic materials. Nat. Rev. Phys. 1, 646 (2019).

[2] Klein, D. R., et al. Probing magnetism in 2D van der Waals crystalline insulators via electron tunneling. Science 360, 1218 (2018).

[3] Song, T., et al. Voltage control of a van der Waals spin-filter magnetic tunnel junction. Nano Lett. 19, 915 (2019).

[4] Zomer, P. J., et al. Fast pick up technique for high quality heterostructures of bilayer graphene and hexagonal boron nitride. Appl. Phys. Lett. 105, 013101 (2014).

[5] Zhang, Z., Shang, J., Jiang, C., et al. Direct Photoluminescence Probing of Ferromagnetism in Monolayer Two-Dimensional $CrBr_3$. Nano Lett. 19, 3138 (2019).

Small Devices for Photo-Induced Electrochemical Synthesis

CNF Project Number: 900-00

Principal Investigator(s): Paul L. McEuen[1,2]

User(s): Samantha L. Norris[1], Yanxin Ji[1], Jonas Rein[3], Song Lin[3]

Affiliation(s): 1. Laboratory of Atomic and Solid State Physics, Cornell University, Ithaca NY, USA;
2. Kavli Institute at Cornell for Nanoscale Science, Cornell University, Ithaca NY, USA;
3. Department of Chemistry and Chemical Biology, Cornell University, Ithaca NY, USA

Primary Source(s) of Research Funding: Cornell Center for Materials Research with funding from the NSF MRSEC program (DMR-1719875), Air Force Office of Scientific Research (AFSOR) multidisciplinary research program of the university research initiative Grant FA2386-13-1-4118

Contact: plm23@cornell.edu, sn588@cornell.edu, yj323@cornell.edu

Primary CNF Tools Used: Heidelberg mask writer - DWL2000, ABM contact aligner, Oxford 81/82/100/Cobra etchers, AJA sputter deposition tool, Oxford PECVD, hot press, Unaxis 770 deep Si etcher

Abstract:

We present microscopic (hundred-micron scale) wireless electrochemical synthesizers that allow for high throughput experimentation (HTE) of small (<100 uL) volumes, allowing for more rapid development of electrochemical synthesis methods in the pharmaceutical industry. Current methods of electrochemical HTE for drug synthesis require epoxying macroscopic electrodes to a custom printed circuit board, placing a lower limit on the reaction volume and limiting the ability to scale to 96- or 384- well plates. In contrast, these Small devices for Photo-induced ElectroChemical Synthesis (SPECS) are individually manipulable and optically powered, allowing for more efficient parallelization of the drug synthesis process.

Summary of Research:

SPECS allow for completely wireless electrochemical synthesis. These devices are fabricated using standard photolithographic techniques, and thus can be produced at the wafer scale. The only serial process in SPECS fabrication is their individual manipulation after separation from the substrate, which is easily automated with a commercial pick-and-place tool.

This technology uses microscale silicon photodiodes connected in series with two electrodes to convert incident light to a current and voltage that can be used to induce electrochemical synthesis at the electrodes. The entire device is encapsulated in 1 uL of silicon dioxide except for the electrode surface which remains exposed to the environment. Under an illumination intensity of about 100 nW/μm^2 at 532 nm, a 100 μm diameter device consisting of seven photodiodes can produce about 20 μA and and 4.5V. The current produced by the SPECS increases linearly with incident light intensity and device area, with the voltage increasing linearly with the number of photodiodes in series — this allows the device to be tailored to the desired synthesis process while still allowing for *in situ* tuning.

To create the silicon photodiode devices, we begin by selectively doping the top of the SOI device layer with phosphosilicate glass to create a vertical PN junction. We then electrically isolate the photodiodes by dry etching to the buried oxide layer in the Oxford Cobra inductively coupled plasma (ICP) etcher. We then connect the photodiodes in series to each other and the electrodes, also conformally coating the silicon defining the electrodes in metal at this step. The metal electrodes and interconnects are platinum with a titanium adhesion layer deposited in the AJA sputter deposition tool.

We encapsulate the photodiodes with silicon dioxide with the Oxford plasma enhanced chemical vapor deposition tool, leaving the metal electrodes protruding (Figure 1).

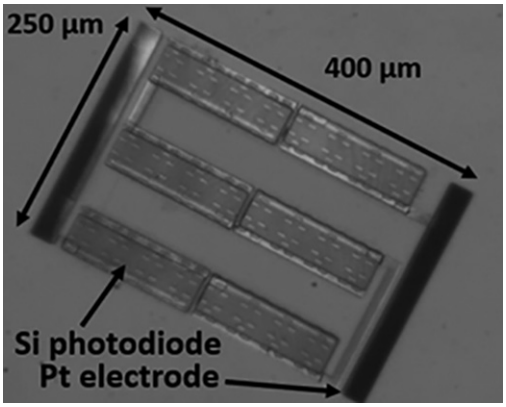

Figure 1: A prototype SPECS device, with six photovoltaic panels and one platinum electrode on each end.

We then sputter and pattern aluminum over the entire device except for the center of the photodiodes. This prevents light from passing through the transparent sections of the device during experiments, which could result in unintended photo-induced synthesis of the reaction mixture.

Due to using planar lithographic techniques to create the SPECS, they are 5 μm thick as fabricated. These thin devices can be released from the substrate by patterning aluminum over them, undercutting the silicon underneath with XeF_2, and then releasing in wet aluminum etchant. After releasing in fluid, the devices are easily pipetted into any container for experimentation (Figure 2). Preliminary results have been achieved with these devices (Figure 3).

To increase rigidity of larger (mm-scale) devices, we transfer them to a transparent substrate. To accomplish this, we bond the wafer with the onboard SPECS to a transparent carrier wafer using a low melting-point thermal plastic polymer and then remove the silicon handle substate via ICP dry etching in the Unaxis 770 Si deep etcher. In the end, we attach the carrier wafer/SPECS stack to a glass substrate and remove the carrier substrate by melting the bonding polymer, followed by dicing to separate the individual devices.

Future work includes electrochemical synthesis using these larger and more rigid SPECS, as well as characterization of their rigidity during sonication, stirring, and other methods of regulating mass transport *in situ*.

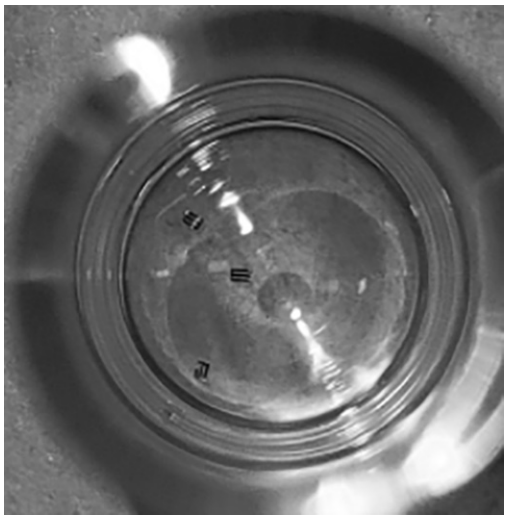

Figure 2: Multiple SPECS after being pipetted into a 5 mm diameter glass vial to be inserted into a 96 well plate.

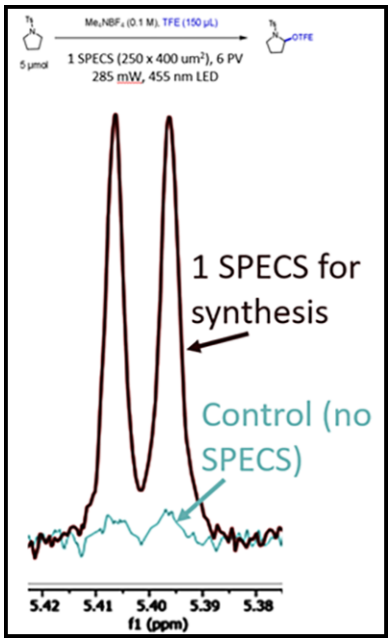

Figure 3: Nuclear magnetic resonance spectroscopy results showing successful Shono oxidation using SPECS, a standard electrochemical synthesis reaction.

Nanofabricated Superconducting Devices for Vortex Dynamics and Qubits

CNF Project Number: 1314-05

Principal Investigator(s): Britton L.T. Plourde

User(s): Brad Cole, Kenneth Dodge, Jaseung Ku, Yebin Liu, Michael Senatore

Affiliation(s): Department of Physics, Syracuse University

Primary Source(s) of Research Funding: Army Research Office

Contact: bplourde@syr.edu, bgcole@syr.edu, krdodgej@syr.edu, jku102@syr.edu, yliu166@syr.edu, masenato@syr.edu

Website: https://bplourde.expressions.syr.edu/

Primary CNF Tools Used: ASML stepper, JEOL 9500, Plasma-Therm 770

Abstract:

We fabricate superconducting microwave devices for studying the dynamics of vortices at low temperatures and for forming novel qubits. Vortices are quantized bundles of magnetic flux that thread many different superconductors over a particular range of applied magnetic field. By using disordered superconducting thin films to form high kinetic inductance wires combined with novel arrays of Josephson junctions, we are able to build structures that can lead to qubits that are protected against decoherence.

Summary of Research:

Superconducting microwave circuits play an important role in quantum information processing. Circuits composed of Josephson junctions and capacitors with superconducting electrodes can serve as qubits, the fundamental element of a quantum computing architecture. Various loss mechanisms limit the ultimate performance of these devices, including trapped magnetic flux vortices. Vortices can be trapped in the superconducting electrodes when background magnetic fields are present and contribute dissipation when driven with microwave currents [1]. Thus, techniques for controlling the trapping of vortices are critical to the development of large-scale quantum information processors with superconducting circuits.

By arranging nanoscale Al-AlOx-Al Josephson tunnel junctions in novel arrays, it is possible to implement new qubit designs that are protected against decoherence [2,3].

We fabricate our microwave resonators from various superconducting films, including aluminum and niobium, deposited onto silicon wafers in vacuum systems at Syracuse University. We define the patterns on the ASML stepper and transfer them into the films with a combination of reactive ion etching and liftoff processing. For defining Josephson junctions, we use the JEOL 9500 along with a dedicated deposition system at Syracuse University. We measure these circuits at temperatures of 100 mK and below in our lab at Syracuse University.

References:

[1] Song, C., Heitmann, T.W., DeFeo, M.P., Yu, K., McDermott, R., Neeley, M., Martinis, John M., Plourde, B.L.T.; "Microwave response of vortices in superconducting thin films of Re and Al"; Physical Review B 79, 174512 (2009).

[2] Doucot, B., Ioffe, L.; "Physical implementation of protected qubits"; Reports on Progress in Physics 75, 072001 (2012).

[3] Dodge, K., Liu, Y., Cole, B., Ku, J., Senatore, M., Shearrow, A., Zhu, S., Abdullah, S., Klots, A., Faoro, L., Ioffe, L., McDermott, R., Plourde, B.; "Protected C-Parity Qubits Part 1: Characterization and Protection"; Bull. Am. Phys. Soc. 2021, http://meetings.aps.org/Meeting/MAR21/Session/X31.3.

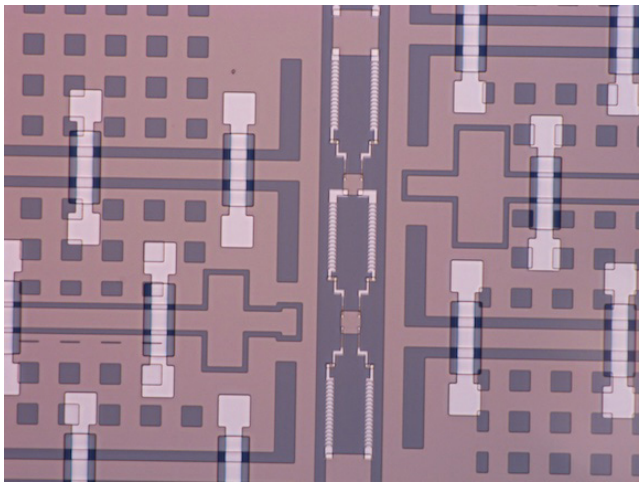

Figure 1: Optical micrograph of plaquette structures formed from arrays of Al-AlOx-Al Josephson junctions for protected qubit design with Nb ground plane and Al/SiOx ground straps.

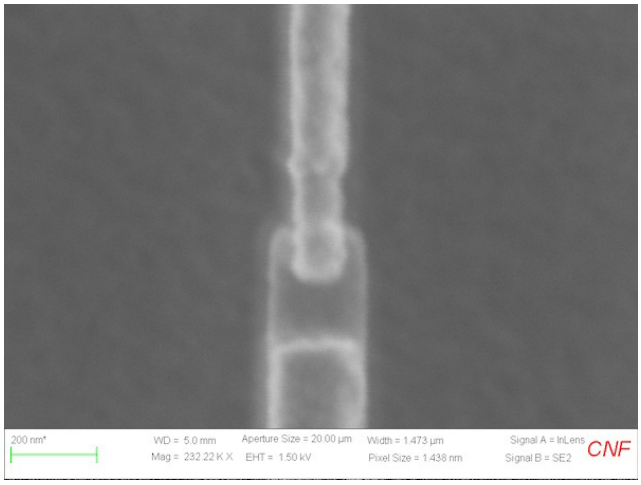

Figure 2: Scanning electron micrograph image of small-area Al-AlOx-Al Josephson junction on protected qubit element.

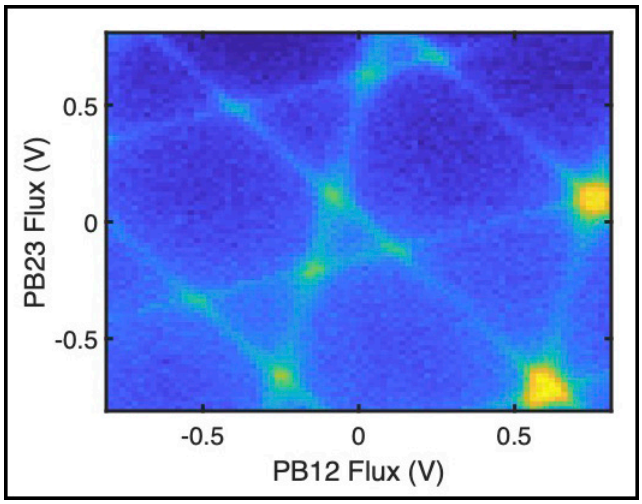

Figure 3: Two-dimensional flux bias voltage modulation of resonant frequency for readout microwave resonator coupled to qubit.

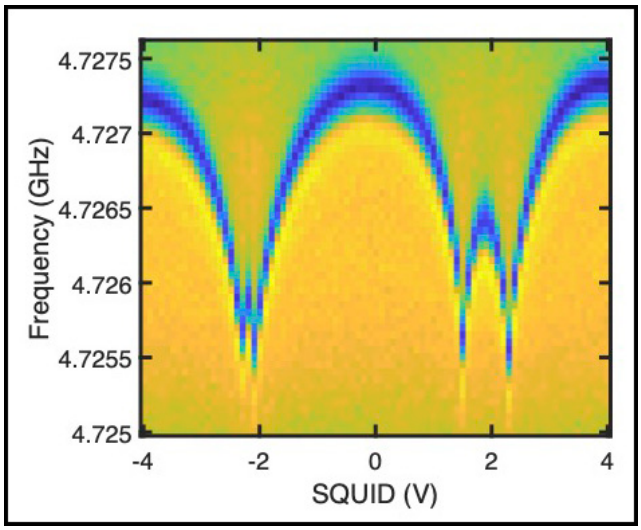

Figure 4: Modulation of qubit transition frequency with flux bias voltage of SQUID tuning loop.

Fabrication of Nanoscale Josephson Junctions for Quantum Coherent Superconducting Circuits

CNF Project Number: 1735-08

Principal Investigator(s): Britton L.T. Plourde

User(s): Andrew Ballard, Brad Cole, Vito Iaia, Indrajeet, Tianna McBroom, Michael Senatore

Affiliation(s): Department of Physics, Syracuse University

Primary Source(s) of Research Funding: Air Force Research Lab, Air Force Office of Scientific Research

Contact: bplourde@syr.edu, alballar@syr.edu, bgcole@syr.edu, vmiaia@syr.edu, indraje@syr.edu, tamcbroo@syr.edu, masenato@syr.edu

Website: https://bplourde.expressions.syr.edu/

Primary CNF Tools Used: ASML stepper, JEOL 9500, Plasma-Therm 770

Abstract:

We fabricate nanoscale superconductor tunnel junctions and other structures for experiments involving quantum coherent circuits. Such circuits have shown great promise in recent years for explorations of quantum mechanics at the scale of circuits on a chip and for forming qubits, the foundational elements of a quantum computer. The quantum state of these superconducting qubits can be manipulated with microwave radiation at low temperatures. We are currently developing superconducting metamaterial structures with novel microwave mode spectra for coupling to superconducting qubits.

Summary of Research:

The unique properties of nanoscale Josephson junctions enable a wide range of novel superconducting circuits for investigations in many diverse areas. In recent years, circuits composed of such junctions have emerged as promising candidates for the element of a quantum computer, due to the low intrinsic dissipation from the superconducting electrodes and the possibility of scaling to many such qubits on a chip [1]. The quantum coherent properties of the circuits are measured at temperatures below 50 mK with manipulation of the qubit state through microwave excitation.

We are developing multimode microwave resonators using combinations of superconducting lumped-circuit elements to engineer metamaterial transmission lines. These structures exhibit novel mode structures characteristic of left-handed materials [2]. We are fabricating such metamaterial transmission lines from Al and Nb films on Si and characterizing these at low temperatures [2]. We are working on experiments to couple these left-handed lines to superconducting qubits for experiments involving the exchange of microwave photons [3,4].

We pattern these circuits at the CNF with nanoscale structures defined with electron-beam lithography on the JEOL 9500 integrated with photolithographically defined large-scale features. The junctions are fabricated using the standard double-angle shadow evaporation technique, in which a resist bilayer of copolymer and PMMA is used to produce a narrow PMMA airbridge suspended above the substrate. Evaporation of aluminum (Al) from two different angles with an oxidation step in between forms a small Al-AlOx-Al tunnel junction from the deposition shadow of the airbridge. We have developed a process for defining these junctions with electron-beam lithography and we perform the aluminum evaporations in a dedicated chamber at Syracuse.

We pattern large-scale features using the ASML stepper, with electron-beam evaporation of Al and sputter-deposition of Nb.

Measurements of these circuits are performed in cryogenic systems at Syracuse University, including dilution refrigerators for achieving temperatures below 30 mK.

References:

[1] Clarke, J. and Wilhelm, F.K.; "Superconducting quantum bits"; Nature, 453, 1031 (2008).

[2] Wang, H., Zhuravel, A., Indrajeet, S., Taketani, B., Hutchings, M., Hao, Y., Rouxinol, F., Wilhelm,F., LaHaye, M.D., Ustinov, A., Plourde, B.; "Mode Structure in Superconducting Metamaterial Transmission Line Resonators"; Physical Review Applied 11, 054062 (2019).

[3] Indrajeet, S., Wang, H., Hutchings, M.D., Taketani, B.G., Wilhelm, F.K., LaHaye, M.D., Plourde, B.L.T.; "Coupling a Superconducting Qubit to a Left-Handed Metamaterial Resonator"; Phy.Review Applied 14, 064033 (2020).

[4] McBroom, T.A., Indrajeet, S., Cole, B.G., Plourde, B.; "Superstrong coupling between a transmon and a metamaterial resonator"; Bull. Am. Phys. Soc. 2021, http://meetings.aps.org/Meeting/MAR21/Session/R30.7.

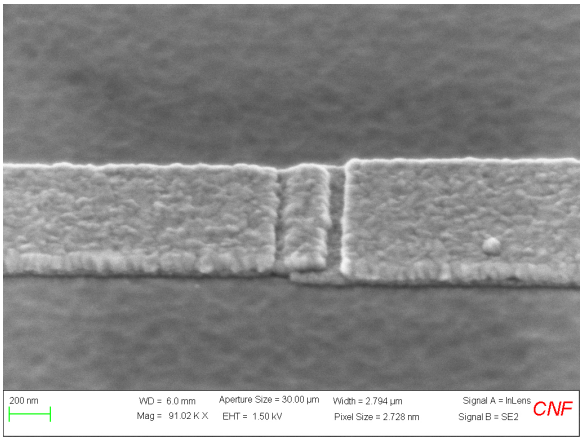

Figure 1: Scanning electron micrograph of Al-AlOx-Al Josephson junction for superconducting qubit.

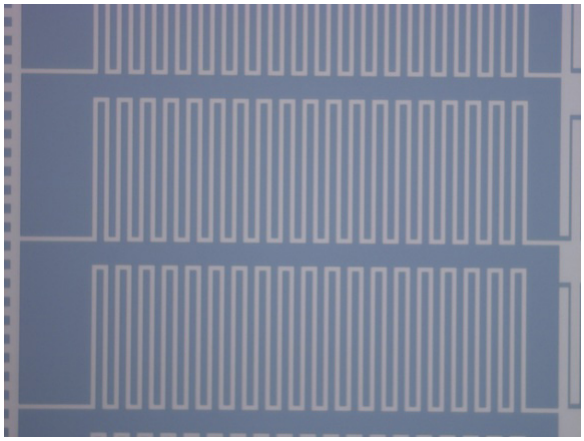

Figure 2: Optical micrograph of Nb meander-line inductor on superconducting metamaterial transmission line resonator.

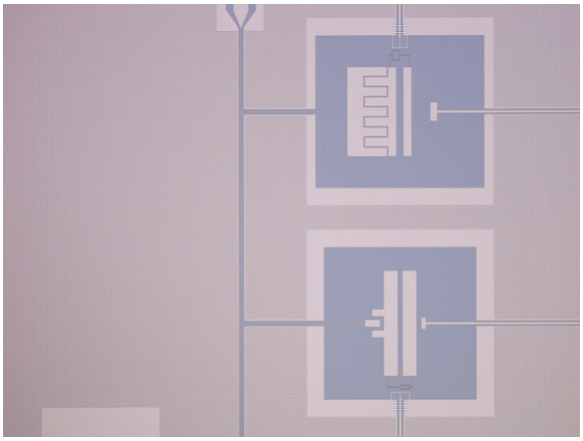

Figure 3: Optical micrograph of superconducting qubits coupled to metamaterial transmission line resonator fabricated from Nb thin film on Si.

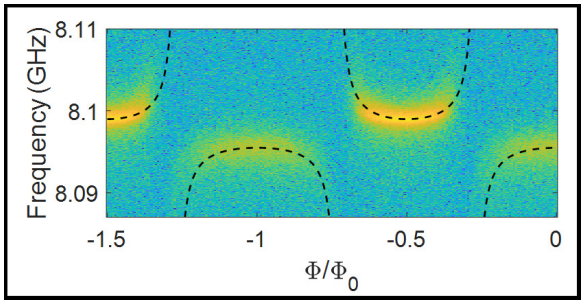

Figure 4: Spectroscopic measurement of microwave transmission through metamaterial transmission-line resonator mode vs. flux modulation of qubit transition frequency.

Nanoscale Magnetization and Current Imaging using Time-Resolved Scanning-Probe Magneto-Thermal Microscopy

CNF Project Number: 2091-11

Principal Investigator(s): Gregory D. Fuchs

User(s): Chi Zhang

Affiliation(s): Applied and Engineering Physics, Cornell University

Primary Source(s) of Research Funding: Air Force Office of Scientific Research (FA9550-14-1-0243, FA9550-18-1-0408), DOE Office of Science, Basic Energy Science (DE-SC0019997)

Contact: gdf9@cornell.edu, cz435@cornell.edu

Primary CNF Tools Used: JEOL 9500, GCA 5x stepper

Abstract:

High resolution, time-resolved magnetic microscopy is crucial for understanding novel magnetic phenomenon such as skyrmions, spin waves, and domain walls. Currently, achieving 10-100 nanometer spatial resolution with 10-100 picosecond temporal resolution is beyond the reach of table-top techniques. We have developed a time-resolved near-field magnetic microscope-based on magneto-thermal interaction, which achieved a spatial resolution on the scale of 100 nm and a temporal resolution below 100 ps. Our results suggest a new approach to nanoscale spatiotemporal magnetic microscopy in an accessible, table-top form to aid in the development of high-speed magnetic devices.

Summary of Research:

Our group has previously developed time-resolved magneto-thermal microscopy for magnetic imaging [1-3]. We apply a pulsed laser to create thermal gradient ∇T. The local magnetization M subjected to ∇T generates an electric field E_{ANE} through the anomalous Nernst effect [Figure 1]. This technique can be used to image both local static and dynamic magnetization, as well as an applied current density [4]. In this work, we extend magneto-thermal microscopy to nanoscale resolution with near-field light. We use a gold-coated cantilever glued on tuning fork as our probe, controlled by atomic force microscopy. We shine a laser on the tip apex, and the near-field enhancement of the electric field at the tip [5-6] heats the sample as a nanoscale heat source [Figure 1]. The heating length scale is comparable to the tip radius, below 100 nm.

We first study a 5 μm × 15 μm CoFeB/Hf/Pt sample fabricated using photolithography with the GCA 5× stepper. We demonstrate magnetic imaging of near-field scanning probe with a multi-domain state. Figure 2(a) shows a far-field image taken using a focused light to confirm the magnetic state. Figures 2(b-d) show topography, far-field and near-field images, acquired simultaneously with the scanning probe. The near-field image resembles the far-field image, but with higher resolution. We note that the smallest feature of the near-field image is ~ 455 nm in this sample, which is below the optical diffraction limit of the set-up. That feature is likely the actual domain wall width rather than being limited by the instrument resolution.

To probe instrument resolution further, we measure in current imaging mode and use a new sample designed with a sharp current density feature. The sample is a thin-film heterostructure composed of 5 nm $Ni_{81}Fe_{19}$/2 nm Ru, then patterned into a 2 μm-diameter disk with two 150 nm necks using JEOL 9500 e-beam lithography. Figure 3 shows topography and near-field current density images taken with the near-field scanning probe. By taking linecuts through two necks, as shown in Figure3(a) inset, we compare signals between focused light far-field and scanning probe near-field microscopy. The scanning near-field image has higher resolution than the far-field image, and by fitting to a model, we demonstrate a spatial resolution on the scale of 100 nm. We note that the resolution here is only an upper bound. We expect a resolution of 50 nm using magneto-thermal microscopy with sharp, high-endurance tips.

We now turn our attention to characterizing the temporal resolution of our instrument. In the measurements, we electrically mix the voltage pulses generated from the sample with reference voltage pulses that are synchronized with the laser but have a controllable delay τ. Figure 4(a) and (b) show the mixed output signal as a function of the delay τ, which can be understood as the temporal convolution signal of the two pulses. The convolved signal widths are roughly 100 ps, similar to the reference pulse width. Therefore, the voltage pulses generated by the near-field thermal excitations must be shorter than 100 ps, demonstrating a time-resolved nano-probe. The picosecond temporal

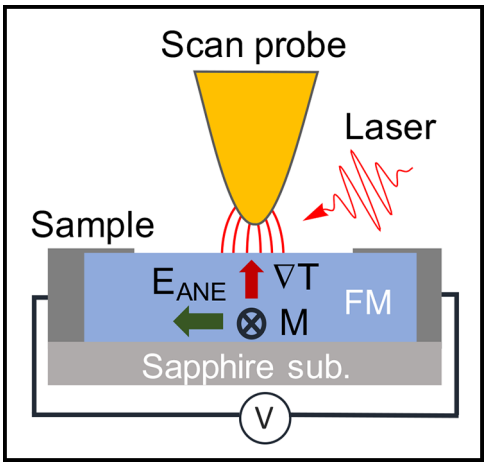

Figure 1: Schematic of scanning near-field magneto-thermal microscopy setup, illustrating laser, sample, scan probe, and near-field interaction.

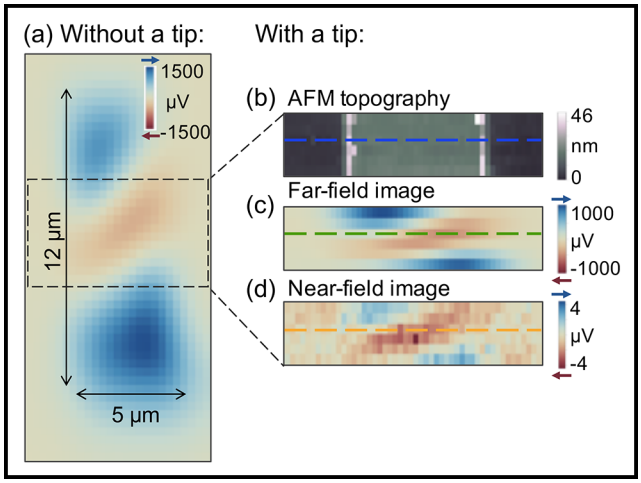

Figure 2: Magnetic multi-domain imaging. (a) Magnetic far-field images of a multi-domain state. With a scanning probe tip, (b) topography, (c) far-field and (d) near-field images acquired simultaneously.

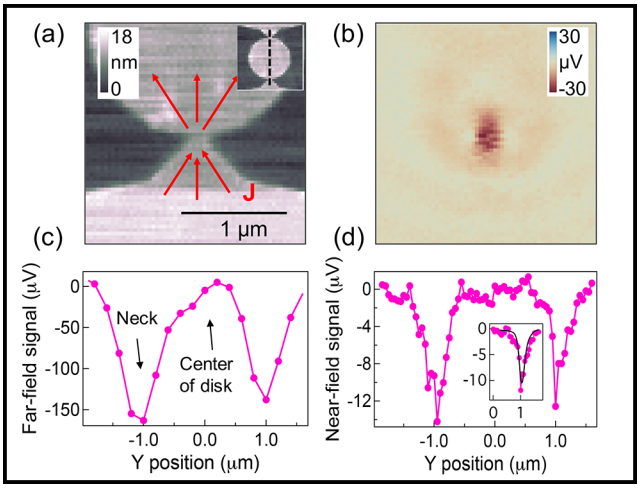

Figure 3: Current imaging and spatial resolution. (a) Topography and (b) current density images. Line cuts of (c) far-field and (d) near-field signals for resolution comparison. (d) The inset shows the simulated fit to the data.

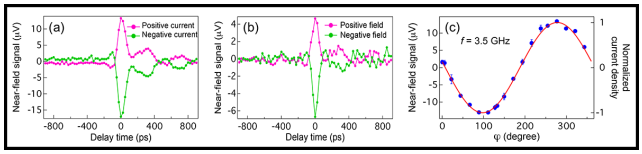

Figure 4: Time-domain measurements of the near-field voltage pulses produced by (a) current density and (b) magnetization as a function of the pulse delay τ. (c) Stroboscopic measurements of microwave current as a function of phase ψ.

resolution enables us to probe a stroboscopic section of the gigahertz frequency cycle. We demonstrate the stroboscopic capability of the scanning probe by measuring a 3.5 GHz microwave current at the nano-constriction. We phase-lock the laser and microwave current such that the thermal pulses constantly probe the current at the same phase ψ. Figure 4(c) shows normalized microwave current density as a function of ψ, showing the phase-sensitive response.

Conclusions and Future Steps:

We have developed a time-resolved scanning near-field magneto-thermal microscopy for magnetic and current imaging. We demonstrated 100 nm scale spatial resolution and picosecond temporal resolution. Next step, we will apply this instrument to study the dynamics of nanoscale spin textures, e.g. magnetic skyrmions.

This work is published in Nano Letters in Ref. [7].

References:

[1] J. M. Bartell, D.H. Ngai, et al., Nat. Commun. 6, 8460 (2015).

[2] J. M. Bartell, et al., Phys. Rev. Appl. 7, 044004 (2017).

[3] I. Gray, et al., Phys. Rev. Mater. 3, 124407 (2019).

[4] F. Guo, et al., Phys. Rev. Appl. 4, 044004 (2015).

[5] J. C. Karsch, et al., APL Photonics 2, 086103 (2017).

[6] L. Meng, et al., Optics Express, 11, 13804, (2015).

[7] C. Zhang, et al., Nano Lett. 21, 4966 (2021).

Strain Tuning of Quantum Emitters in Monolayer Transition Metal Dichalcogenides

CNF Project Number: 2126-12

Principal Investigator(s): Gregory Fuchs

User(s): Jaehong Choi

Affiliation(s): Applied and Engineering Physics, Cornell University

Primary Source(s) of Research Funding: Air Force Office of Scientific Research Multidisciplinary Research Program of the University Research Initiative (AFOSR MURI)

Contact: gdf9@cornell.edu, jc3452@cornell.edu

Primary CNF Tools Used: JEOL 6300, 5X g-line stepper, Oxford COBRA, Oxford 81, DISCO dicing saw, CVC SC4500 odd hour evaporator, Veeco Icon AFM, wire bonder, Heidelberg mask writer - DWL2000

Abstract:

Tensile strain has been known to modulate the band gap of two-dimensional (2D) transition metal dichalcogenides (TMDs), which effectively funnels excitons and activates quantum emitters in a deterministic way. We used an array of cylindrical nanopillars to create quantum emitters and discovered that single photon emitters with high purity are often formed on wrinkles rather than on the pillar apex. We also studied strain-tuned interlayer excitons in heterobilayers of 2D TMDs. We discovered that the strain exerted by nanopillars activates interlayer excitons in WSe_2/WS_2 heterobilayers irrespective of twist angles. We confirmed that the strain profile of the pillar apex is complex and that spectra associated with the pillar apex have multiple emission peaks with higher background. Wrinkles formed around the pillars, on the other hand, often generate spectra with lower background.

Summary of Research:

Monolayer transition metal dichalcogenides (TMDs) have been actively studied for quantum technology and optoelectronics due to their unique properties such as strong excitonic binding, a direct band gap, and spin-valley locking [1]. It has been shown that tensile strain modulates the band structure of 2D TMDs [2-4]. Site-localized tensile strain reduces the local band gap enabling excitons to be funneled into the strain potential before recombination, leading to single photon emission. Nanostructures such as nanopillars [2-3], nanorods [5], and nanobubbles [6] have been used to deterministically activate single photon emitters through this strain confinement. However, the strain induced by these nanostructures often have complex profiles and this typically results in multiple confining sites or large confining potential that hampers the single photon emission.

Our group has strain-tuned monolayer WSe_2 with cylindrical nanopillars and discovered that the wrinkle formed nearby the nanopillar gives rise to single photon emitters with higher purity as with compared to the emitters from the pillar apex (Figure 1) [7].

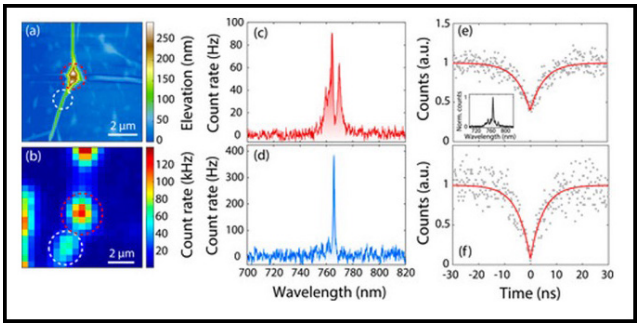

Figure 1: Comparison between pillar emission and wrinkle emission on WSe_2 stacked on nanopillars. (a) Atomic force microscopy image showing a pillar and wrinkles, (b) Photoluminescence map of the pillar (red) and wrinkle (white), (c),(e) spectrum and g2 measurement of emitters from the pillar apex. (d),(f) spectrm and g2 measurement of emitters from the wrinkle [7].

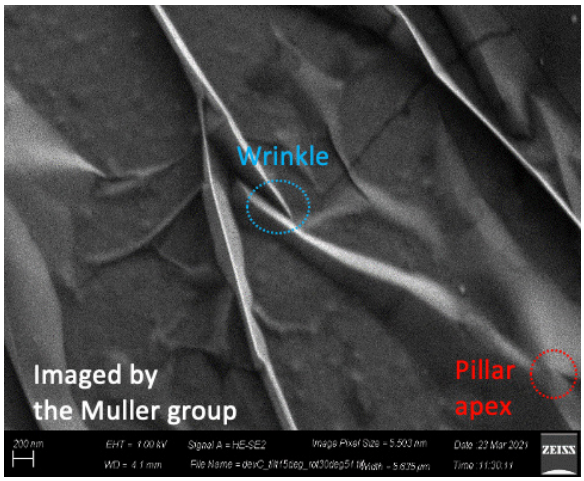

Figure 2: Scanning electron microscopy image of wrinkles formed on h-BN/WSe_2. The sharp folds on the wrinkle (blue) often exhibit sharp emission peaks.

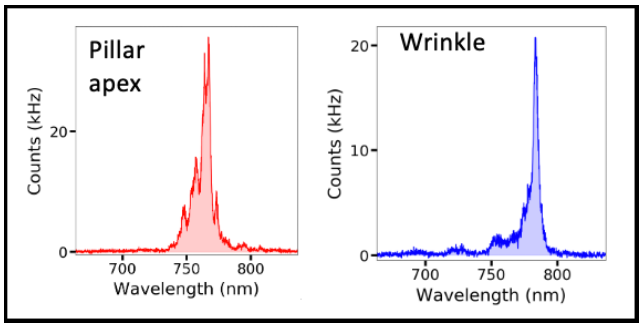

Figure 3: Spectra of interlayer excitons associated with the pillar apex (red) and wrinkle (blue).

The physics behind this finding can be better understood by quantifying the strain profile on the pillar apex and the wrinkle. With high resolution electron microscopy in collaboration with Professor David Muller's group, we found out that wrinkles with a sharp fold gives rise to single photon emitters with high purity (Figure 2). The characteristics of the strain exerted by wrinkles can be further explored by quantifying the strain gradient via electron microscopy, and this is in progress.

We also used nanopillars to activate interlayer excitons in a WSe_2/WS_2 heterobilayer. When two different TMD monolayers are stacked together, the electrons and holes find their energy minima in the composite material. When a bilayer is engineered such that the composite layer forms a type II band alignment, the coulomb-bound electron and hole can be separated into different layers. It has been found that the photoluminescence intensity of interlayer excitons is enhanced at 0° and 60° alignment angles, but significantly suppressed at intermediate angles due to the momentum mismatch [8]. We stacked WSe_2/WS_2 heterobilayer onto nanopillars and studied the strain effect.

We found that strain-tuned interlayer excitons exhibit fairly high photoluminescence intensity at any twist angle, which implies that momentum matching is not necessary when interlayer excitons are confined by the strain potential. We also observed that the spectra associated with wrinkles often exhibit sharper peaks with lower background compared to those associated with pillar apex (Figure 3), which is consistent with our work on monolayer WSe_2 [7].

Conclusions and Future Steps:

Nanopillars create a strain potential that confines excitons. We discovered that the emitters formed on wrinkles produce spectra with low background and sharp emission peaks. Also, strain-confined interlayer excitons exhibit high photoluminescence intensity irrespective of twist angle. Our next step is to quantify the strain profile on the wrinkle via electron microscopy, which will allow us to better understand the physics of wrinkles and design high-quality emitters more deterministically.

References:

[1] Mak, K., Shan, J., Nat. Photon 10, 216-226 (2016).

[2] Palacios-Berraquero, C., et al. Nat Commun 8, 15093 (2017).

[3] Branny, A., et al. Nat Commun 8, 15053 (2017).

[4] Chaves, A., et al. npj 2D Mater Appl 4, 29 (2020).

[5] So, Jae-Pil, et al. Nano Lett 21, 1546-1554 (2021).

[6] Darlington, T.P., et al. Nat Nanotechnol. 15, 854-860 (2020).

[7] Rapahel S. Daveau, et al. APL Photonics 5, 09615 (2020).

[8] Nayak K. Pramoda, et al. ACS Nano 11, 4, 4041-4050 (2017).

Mechanically Driven Electron Spins with a Diamond Thin-Film Bulk Acoustic Resonator

CNF Project Number: 2126-12

Principal Investigator(s): Gregory Fuchs[1]

User(s): Johnathan Kuan[2], Anthony D'Addario[2]

Affiliation(s): 1. Department of Applied and Engineering Physics, Cornell University; 2. Department of Physics, Cornell University

Primary Source(s) of Research Funding: Defense Advanced Research Projects Agency-DARPA DRINQS program (Cooperative Agreement #D18AC00024)

Contact: gdf9@cornell.edu, jk2788@cornell.edu, ajd344@cornell.edu

Website: https://fuchs.research.engineering.cornell.edu/

Primary CNF Tools Used: OEM Endeavor M1, Westbond 7400A ultrasonic wire bonder

Abstract:

Lattice strain has been demonstrated to be an effective method of coherently manipulating electron spins in solid state defect centers such as the diamond nitrogen-vacancy center. In previous experiments, strain is introduced into the diamond lattice through a high overtone bulk acoustic resonator (HBAR). To improve the strain and power efficiency of bulk acoustic resonators for quantum control, we develop and characterize a diamond thin-film bulk acoustic resonator. We measure the electromechanical performance of the device and demonstrate coherent driving of a double quantum transition a nitrogen-vacancy center (NV) of electron spin ensemble.

Summary of Research:

The diamond nitrogen-vacancy (NV) center is a well characterized solid state defect center consisting of a substitutional nitrogen impurity adjacent to a lattice vacancy. The NV center electron spin interacts with many external fields (magnetic, electric, etc.), making it an excellent platform for quantum sensing. In addition to the electron spin, the NV center has a native nitrogen nuclear spin, which is coupled to the electronic spin through a hyperfine interaction. This provides an opportunity to use the nuclear spin for sensing applications, with state preparation and readout facilitated by the electron spin. However, the hyperfine interaction also provides an additional source of decoherence for the nuclear spin, limiting the sensitivity of any potential quantum sensing protocols employing these spins. It has been shown that strong driving of the electron spin can help protect the coherence of the nuclear spin [1]. Previous experiments with high overtone bulk acoustic resonators (HBAR) on diamond have demonstrated electron spin driving with lattice strain for coherent control [2], and continuous dynamical decoupling for protecting electron spin coherence [3].

To achieve strong driving of the electron spin with lattice strain, we fabricate thin-film bulk acoustic resonators (FBAR) on single crystal diamond (Figure 1). The FBAR resonators consist of a 1.5 μm AlN transducer, with a bottom (Al) electrode and a top (Pt) electrode. The transducer is deposited onto a 10 μm thick optical grade diamond, which is created through reactive ion etching. The AlN film is sputtered using the OEM Endeavor M1 tool at CNF. Compared to previous generations of ZnO HBAR on diamond, the AlN diamond FBAR has better power handling, which allows for much stronger acoustic driving of electron spins by simply applying more power. To provide microwave control of the spins, we also fabricate a loop antenna, which surrounds the FBAR.

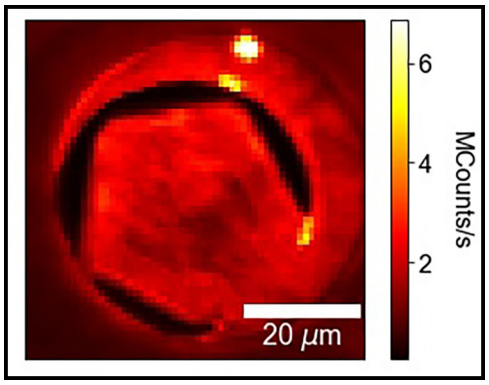

Figure 1: Photoluminescence image of an AlN FBAR on diamond. The FBAR (pentagonal feature) consists of a 1.5 μm AlN film that is sandwiched by an Al bottom electrode and a Ti/Pt top electrode. This stack is on top on a 10 μm diamond membrane.

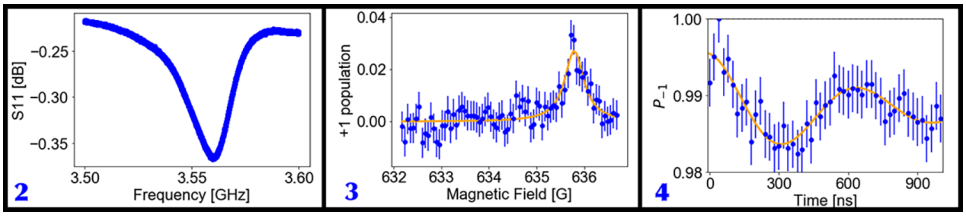

Figure 2, left: S11 measurement of the 3.56 GHz acoustic mode of the AlN FBAR. Figure 3, middle: Spectroscopy of the double quantum transition. The resonator frequency is fixed at 3.56 GHz while the Zeeman splitting between the ms = -1 and ms = +1 states is swept. The peak at approximately 636 G gives the external field necessary to tune the double quantum transition in resonance with the acoustic mode. Figure 4, right: Rabi driving of the double quantum transition with a Rabi field of 1.7 MHz.

We measure the electromechanical resonances of the AlN FBAR by measuring the S11 response with a vector network analyzer. To characterize the device, we focus on an acoustic mode at 3.56 GHz (Figure 1) with a low quality factor (~10). We coherently drive a double quantum transition (ms = -1 to ms = +1) with this mode to measure the lattice strain in the diamond. To ensure that the acoustic mode is resonantly driving the electron spin, we perform spectroscopy where the Zeeman splitting between ms = -1 to ms = +1 is swept [3]. This locates the correct external magnetic field to apply along the NV symmetry axis, which will tune the electron spin transition in resonance with the acoustic mode. Using this field, we drive Rabi oscillations of the electron spin using acoustic pulses and measure the strain in the FBAR through the Rabi frequency [4]. In this device, we drive the electron spin using an electromechanical mode at 3.5 GHz. The measured Rabi field from the oscillations is 1.7 MHz, which is comparable with the hyperfine splitting of the NV center (2.1 MHz).

Conclusions and Future Steps:

We have developed a process for fabricating AlN FBARs on diamond to drive electron spins. To improve the acoustic driving, we aim to improve the quality factor of the resonator. This can be achieved by adjusting the dimensions of the resonator and the diamond substrate. In addition, we are looking at optimizing this process for isotopically pure CVD diamond. Isotopically pure diamond can host NV centers with phase coherence times on the order of 10 μs, making it an excellent substrate for developing a quantum sensor.

References:

[1] M Chen, W. K. C. Sun, K Saha, J. Jaskula, and P. Cappellaro. "Protecting solid-state spins from a strongly coupled environment". New Journal of Physics 20.6 (2018).

[2] E. R. MacQuarrie, T. A. Gosavi, A. M. Moehle, N. R. Jungwirth, S. A. Bhave, and G. D. Fuchs, Coherent control of a nitrogen-vacancy center spin ensemble with a diamond mechanical resonator, Optica 2, 233 (2015).

[3] E. R. MacQuarrie, T. A. Gosavi, S. A. Bhave, and G. D. Fuchs, Continuous dynamical decoupling of a single diamond nitrogen-vacancy center spin with a mechanical resonator, Phys. Rev. B 92, 224419 (2015)

[4] E. R. MacQuarrie, T. A. Gosavi, N. R. Jungwirth, S. A. Bhave, and G. D. Fuchs, Mechanical spin control of nitrogen-vacancy centers in diamond, Phys. Rev. Lett. 111, 227602 (2013).

Fabrication of Nanophotonic Optical Cavity Device from Inverse Design

CNF Project Number: 2126-12

Principal Investigator(s): Gregory D. Fuchs[1]

User(s): Jialun Luo[2]

Affiliation(s): 1. School of Applied and Engineering Physics, 2. Department of Physics; Cornell University

Primary Source(s) of Research Funding: National Science Foundation (ECCS-1839196)

Contact: gdf9@cornell.edu, jl3562@cornell.edu

Website: http://fuchs.research.engineering.cornell.edu

Primary CNF Tools Used: AJA sputter deposition, OEM Endeavor AlN sputtering system, JEOL 9500, JEOL 6300, PT770 etcher, AJA ion mill, P10 profilometer, P-7 profilometer, GCA 5x stepper

Abstract:

On-demand polarized single-photons are essential in realizing many photon-based quantum communication protocols [1]. We developed and fabricated a nanophotonic cavity device from aluminum nitride (AlN) whose structure was calculated from an inverse design method. The structure serves as a platform for enhancing the collection of single photons from isolated defects hosted in hexagonal boron nitride (h-BN). We present an update on our work-in-progress on the fabrication of the device.

Summary of Research:

Hexagonal boron nitride is an interesting 2D material due to bright optically active defects hosted within and to the possibilities of integrating with other 2D materials [2]. Researchers have been able to create isolated defects by methods such as ion implantation with carbon [3]. The defects are stable under room temperature and have zero-phonon line fluorescence at 585 nm [4]. People have been able to create or find isolated these defects. The combination of emission brightness and the capability of isolating them makes h-BN defects promising candidates as single-photon sources. In this project, we aim to fabricate an inverse design nanophotonic cavity structure and characterize its capability of enhancing photon emissions. The cavity structure further enhances the emission of h-BN defects placed on them due to the Purcell effect and modifies the emission angle of these defects so one can more efficiently collect the photons [5].

We fabricated the current generation devices on Si wafers, which allows us to cleave the sample and inspect the cross section. The devices are made from AlN sputtered by the OEM Endeaver M1 AlN sputter system. The structure is patterned with the JEOL 9500 electron beam lithography system and is subsequently etched with a Cl_2 plasma reactive ion etching process in the PT770 etcher.

Figure 1 shows (a) the design target structure and (b) the field profile at resonance at 600 nm. Figure 1c shows the mask pattern prior to AlN etching, indicating a good fidelity of patterning from design structure. However, as seen in Figure 1d, the AlN etching step is problematic due to high aspect ratio (15:1) and results in slanted sidewalls and incomplete etching of the interior of the pattern.

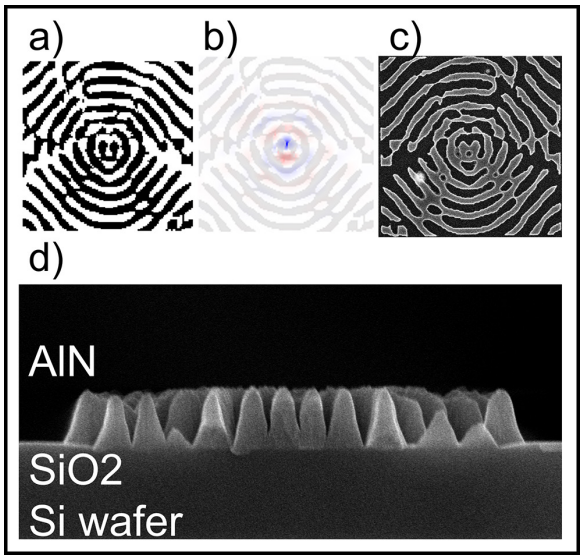

Figure 1: a) The target device structure from inverse design. Black indicates substrate and white air. b) The field mode profile at 600 nm resonance. Note that most of the energy is concentrated at the central region. c) An SEM image of the Cr hard mask before the final AlN etch. d) An SEM image of the cross section of the device.

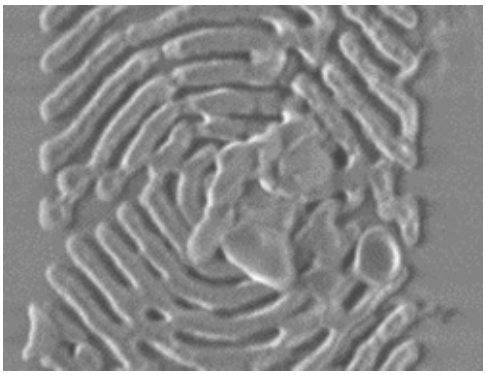

Figure 2: A top-down SEM image of a few h-BN nanoflakes on top of the AlN device.

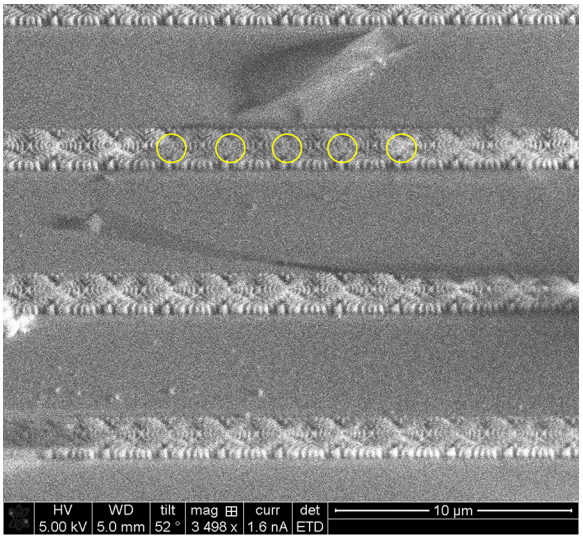

Figure 3: An SEM image of an exfoliated h-BN flake over a few cavity devices. The circles indicate the regions for focused ion beam milling to create defects.

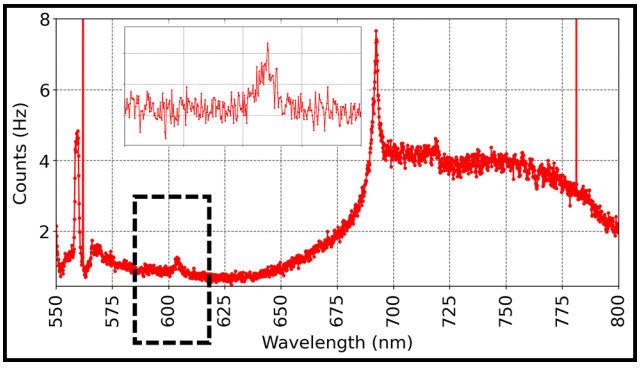

Figure 4: A spectrum taken at the central region of the cavity device. The insert magnifies around the spectral feature around 604 nm.

While we continue to improve the fabrication process, we started testing strategies of placing single emitting h-BN defects on the cavity structure. Figure 2 shows our early attempts of placing h-BN nanoflakes on top of the device through drop-casting sufficiently many of them on a chip containing many of such cavity devices. We also tried placing an exfoliated h-BN flake over the device and creating defects by lightly milling the flake with focused ion beam (Figure 3). Unfortunately, the early attempts did not result in single emitters in the range of the enhancement region. However, we observed an enhancement of the background fluorescence near the device center at 604 nm, which likely comes from the device as shown in Figure 4.

Future Work:

We are exploring ways of creating and positioning single defects in h-BN with better repeatability. We also pursue a different design which optimizes upward photon flux which may achieve a higher photon collection rate.

Acknowledgements:

We would like to thank members of the Rodriguez Group on the discussion on and their designs of the nanophotonic cavity structures.

References:

[1] Bennett, C. H. and Brassard, G. Quantum cryptography: Public key distribution and coin tossing. Theoretical Computer Science 560, 7-11 (2014).

[2] Aharonovich, I., Englund, D., and Toth, M. Solid-state single-photon emitters. Nature Photonics 10, 631-641 (2016).

[3] Mendelson, N., et al. Identifying carbon as the source of visible single-photon emission from hexagonal boron nitride. Nat. Mater. 20, 321-328 (2021).

[4] Jungwirth, N. R. and Fuchs, G. D. Optical Absorption and Emission Mechanisms of Single Defects in Hexagonal Boron Nitride. Phys. Rev. Lett. 119, 057401 (2017).

[5] Molesky, S., et al. Inverse design in nanophotonics. Nature Photonics 12, 659-670 (2018).

Charge-Order-Enhanced Capacitance in Semiconductor Moiré Superlattices

CNF Project Number: 2633-18

Principal Investigator(s): Jie Shan, Kin Fai Mak

User(s): Tingxin Li, Jiacheng Zhu

Affiliation(s): Laboratory of Atomic and Solid State Physics, School of Applied and Engineering Physics; Cornell University

Primary Source(s) of Research Funding: Department of Energy

Contact: jie.shan@cornell.edu, kinfai.mak@cornell.edu, tl684@cornell.edu, jz969@cornell.edu;

Primary CNF Tools Used: Autostep i-line stepper, Hamatech wafer processor develop, Heidelberg mask writer - DWL2000, photolithography spinners, CVC SC4500 odd/even-hour evaporator, DISCO dicing saw

Abstract:

Van der Waals moiré materials have emerged as a highly controllable platform to study the electronic correlation phenomena. In particular, robust correlated insulating states have recently been discovered at both integer and fractional filling factors of the semiconductor moiré systems. In this project, we study the electronic compressibility of $MoSe_2/WS_2$ moiré superlattices by capacitance measurements. Our results reveal the thermodynamic properties and illustrate mechanism for enhanced capacitance in semiconductor moiré superlattices.

Summary of Research:

Quantum capacitance C_Q represents electronic compressibility or thermodynamic density of states of an electronic system that relates to its thermodynamic properties [1]. Quantitative measurement of C_Q can be realized by measuring differential capacitance per unit area C ($C^{-1} = C_g^{-1} + C_Q^{-1}$ with C_g denoting the geometrical capacitance between sample and gate) [2]. Semiconductor moiré superlattices host strongly correlated insulating states [3]. In this project, we demonstrate capacitance measurements on such system, which not only provide thermodynamic quantities but also offer new insight into correlations in van der Waals heterostructures.

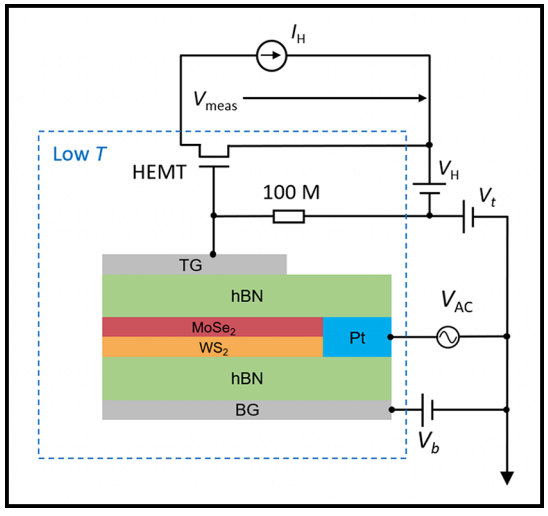

Figure 1: Schematics of a dual-gate device structure and electrical connections for capacitance measurements. TG and BG denote the top and back gate, respectively.

Figure 1 shows the schematics of dual-gated device structures and electrical connections for capacitance measurements. The device is made of an angle-aligned $MoSe_2$ and WS_2 heterobilayer encapsulated by top and bottom graphite gates separated by hexagonal boron nitride (h-BN) dielectrics. Angle-aligned $MoSe_2/WS_2$ heterobilayers form a triangular moiré superlattice with moiré period $a_M \approx 8$ nm due to 4% lattice mismatch between these materials. A commercial high electron mobility transistor (HEMT, model FHX35X) is used as the first-stage amplifier to effectively reduce the parasitic capacitance from cabling [4]. To obtain the top gate capacitance, we apply an AC voltage (10 mV in amplitude) to the moiré superlattice and collected the signal from the top gate through the HEMT.

Figure 2 is an optical image of a typical device. The Pt electrodes are patterned on the Si/SiO_2 substrates by photolithography and metal evaporation. Atomically thin samples of $MoSe_2$, WS_2, h-BN, and graphite are first exfoliated from their bulk crystals onto silicon substrates covered with a 300 nm thermal oxide layer. Selected thin flakes of appropriate thickness and geometry are then picked up one-by-one by a stamp consisting of a thin layer of polycarbonate on polydimethylsiloxane (PDMS). The complete heterostructure is then deposited onto the substrates with pre-patterned Pt electrodes.

Figure 3 shows the measured differential capacitance C in the unit of C_g as a function of top gate voltage measured at 10 K and bottom gate voltage V_b = 5.3 V. We observe a step increase of capacitance around -4 V when the Fermi level enters the conduction band of $MoSe_2$. The capacitance plateaus out above ~ 0 V when the sample is heavily electron doped. We calibrate capacitance using these two limits: $C / C_g = 0$ when the Fermi level lies inside the superlattice band gap (> 1 eV) and the sample is insulating (incompressible); $C / C_g \approx 1$ when the sample is heavily doped and behaves as a good conductor. At intermediate gate voltages, we identify a series of capacitance dips (incompressible states). The most prominent ones appear equally spaced in gate voltage and are assigned integer fillings ν = 1, 2, 3 and 4. The assignment is consistent with the known moiré density and the carrier density n evaluated from the gate voltage and $C_g \approx 2.1 \times 10^{-7}$ Fcm^{-2}. The latter is determined from the permittivity and thickness of the h-BN gate dielectric d ($\varepsilon \approx 3\varepsilon_0$ with ε_0 denoting the vacuum permittivity).

It was independently verified by including a reference capacitor on the measurement chip.

We observe anomalously large capacitance in the compressible regions between the incompressible states. The enhancement is particularly large at small doping densities with C exceeding C_g by ~ 30% for device with $d/a_M \approx 1$. Figure 4 shows devices of different sample-gate separation ($d/a_M \approx 0.6, 0.8, 1.0$ and 1.5). The capacitance enhancement increases with decreasing d/a_M. It is as high as 60% in device with $d/a_M \approx 0.6$ at 10 K.

The experimental results show that the correlation effects are strongly dependent on sample-gate separation in devices with $d/a_M \sim 1$, particularly, for the fractional-filling states since the gate electrodes effectively screen the extended Coulomb interactions. In this regime where electronic interactions dominant and sample gate distance is comparable to electron separations, we need to describe the entire device as one system [5].

In conclusion, our study establishes capacitance as a powerful thermodynamic probe of the correlated states in semiconductor moiré superlattices. It also illustrates the importance of sample-gate coupling and the device-geometry-dependent extended Coulomb interaction at fractional fillings.

References:

[1] Ando, T., Fowler, A. B. and Stern, F. Electronic properties of two-dimensional systems. Rev. Mod. Phys. 54, 437-672 (1982).

[2] Smith, T. P., Goldberg, B. B., Stiles, P. J., and Heiblum, M. Direct measurement of the density of states of a two-dimensional electron gas. Phys. Rev. B. 32, 2696-2699 (1985).

[3] Xu, Y., et al. Correlated insulating states at fractional fillings of moiré superlattices. Nature 587, 214-218 (2020).

[4] Ashoori, R. C., et al. Sigle-Electron Capacitance Spectroscopy of Discrete Quantum Levels. Phys. Rev. Lett. 68, 3088-3091 (1992).

[5] Skinner, B., and Shklovskii, B. I. Anomalously large capacitance of a plane capacitor with a two-dimensional electron gas. Phys. Rev. B 82, 155111 (2010).

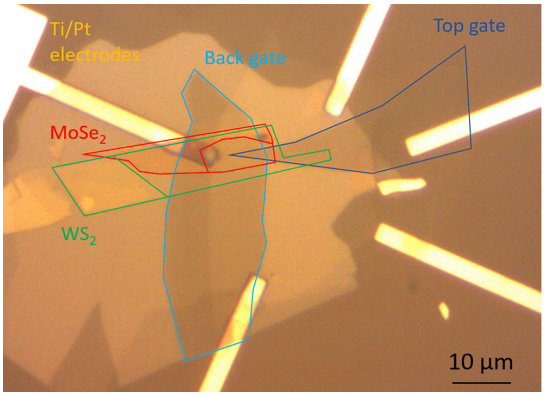

Figure 2: Optical microscope image of a dual-gate device. Colored lines show the boundary of the $MoSe_2$, WS_2, top gate and bottom gate flakes, respectively. Scale bar is 10 μm.

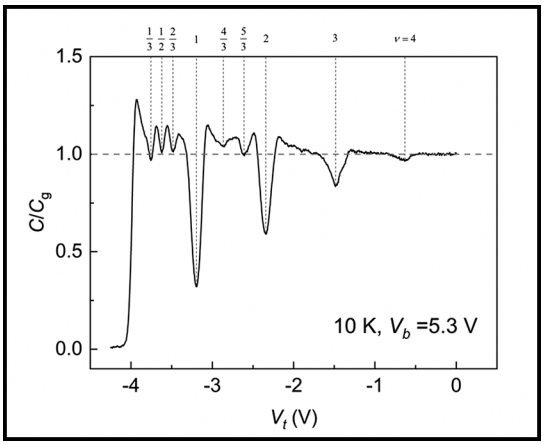

Figure 3: Differential top gate capacitance as a function of top gate voltage at 10 K for Device with $d/a_M \approx 1$. The back gate voltage is fixed at 5.3 V. The filling factors for discernable incompressible states are labeled on the top axis.

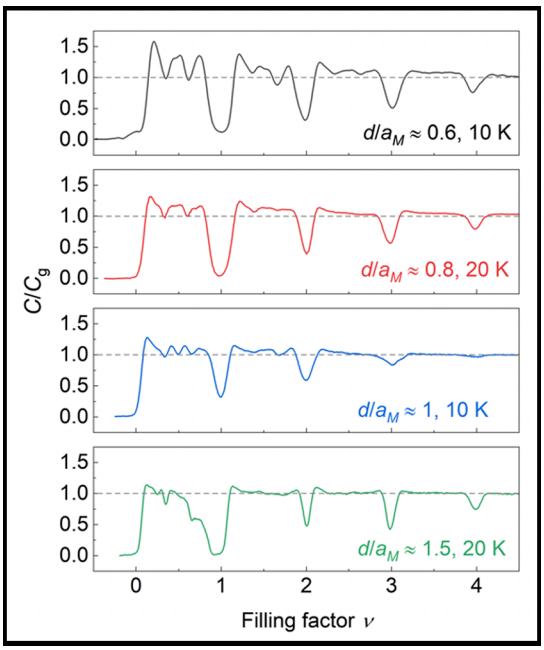

Figure 4: Experimental top gate capacitance as a function of filling factor for devices with $d/a_M \approx 0.6, 0.8, 1.0$ and 1.5 (from top to bottom) at the lowest temperature (10 K or 20 K) allowed by the sample/contact resistance.

Thermal and Electrical Properties of Quasi-1D van der Waals Nanowires

CNF Project Number: 2698-18

Principal Investigator & User: Deyu Li

Affiliation(s): Department of Mechanical Engineering, Vanderbilt University

Primary Source(s) of Research Funding: National Science Foundation

Contact: deyu.li@vanderbilt.edu

Primary CNF Tools Used: Heidelberg mask writer - DWL2000, Autostep i-line stepper, LPCVD nitride - B4, GSI PECVD, AJA sputter deposition, AJA ion mill

Abstract:

Using the microdevices fabricated at CNF, we conducted extensive measurements of thermal transport through quasi-one-dimensional (quasi-1D) van der Waals (vdW) crystal $NbSe_3$ nanowires. Dimensional transition from 3D to 1D was demonstrated when the nanowire diameter scales down below 26 nm. Importantly, we found that one-dimensional (1D) phonons led to superdiffusive transport with the nanowire thermal conductivity becoming divergent with the wire length following a 1/3 power law extending over an unprecedented 42.5 μm. This important result has been published in *Nature Nanotechnology*.

Summary of Research:

Because of the pandemic, no on-site nanofabrication at CNF was conducted during the reporting period. However, using the previously fabricated microdevices, we conducted extensive measurements of thermophysical properties of quasi-1D vdW crystal $NbSe_3$ of different diameters and lengths. The schematic diagram of the measurement scheme, an SEM micrograph of an $NbSe_3$ wire placed on the measurement device, and a TEM micrograph of an ultra-thin nanowire were shown in Figure 1.

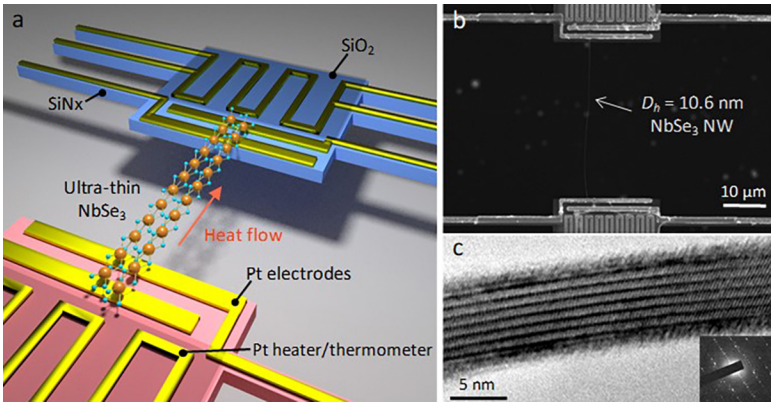

Figure 1: (a) Schematic illustration of the measurement scheme. (b) An SEM micrograph showing a nanowire on the device with a suspended length of 28.2 μm. (c) An HRTEM image of an ultra-thin $NbSe_3$ nanowire showing the crystalline structure.

These measurements have led to a major breakthrough with the first experimental observation of superdiffusive transport of 1D phonons, which has been published in *Nature Nanotechnology* [1].

In 1955, Fermi, Pasta, Ulam, and Tsingou reported their "shocking little discovery" that an excited vibration mode in single atomic chains did not dissipate into heat over a long period of time, which attracted tremendous attention due to its broad implications. A direct consequence of this discovery is that the thermal conductivity of 1D lattices becomes divergent with the chain length, suggesting a type of thermal superconductors of ever-increasing thermal conductivity with the sample length.

The concept remains purely conceptual and is regarded as of academic interest only as single atomic chains of sufficient length remain experimentally unattainable.

Our study shows that the thermal conductivity of ultra-thin $NbSe_3$ nanowires increases with the wire length beyond a record level of 42.5 μm following a 1/3 power law, providing the first experimental evidence for superdiffusive transport.

Figure 2a plots the measured room temperature thermal conductivity (κ) versus the hydraulic diameter (D_h) of the nanowires, with all nanowires of ~ 15 μm long. Interestingly, the data indicate a clear transition at D_h = 26 nm. For thicker wires, κ decreases as D_h reduces due to phonon-boundary scattering; however, as D_h further drops, κ demonstrates an unexpected steep upward trend with ~ 25 fold increase for a 6.8 nm wire.

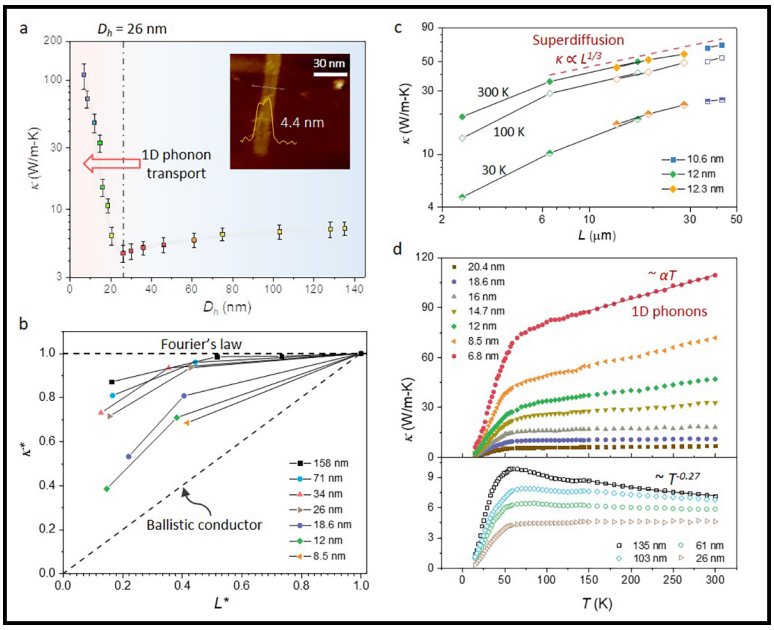

Figure 2: Divergent and superdiffusive transport of 1D phonons. (a) Measured room temperature thermal conductivity (κ) versus the hydraulic diameter (D_h). Inset: AFM scanning profile of the nanowire with D_h = 6.8 nm. (b) Normalized room temperature κ versus the normalized suspended length, which indicates a convergence-divergence transition as D_h decreases. (c) Measured κ versus suspended length at different temperatures. (d) Temperature dependence of κ for different diameter wires.

Next we examine the length dependence of κ, and Figure 2b plots the normalized room temperature thermal conductivity, κ^*, versus the normalized suspended length, L^*, both with respect to the values of the respective longest wires (~ 15 μm), for seven wires of different D_h. Interestingly, for wires with larger D_h, κ first increases with L from ~ 2 to ~ 6 μm, and then converges to a saturated value. However, as D_h reduces to below 26 nm, κ exhibits a much stronger length dependence even for $L > 6\,\mu$m, suggesting a transition from convergence to divergence.

To further explore the length dependence, we measured more samples with much longer suspended length. Figure 2c indicates that for nanowires with D_h in the range of 10 to 12 nm, the length dependence extends beyond 42.5 μm, much larger than the previously reported values for different wires. Interestingly, in the length range of > 6.5 μm, the measured κ follows a trend of $\kappa \propto L^{1/3}$, consistent with the theoretical prediction of superdiffusive phonon transport in 1D lattices.

To further confirm the superdiffusive transport, we also plot the measured κ at 100 K, which again follows the trend of $\kappa \propto L^{1/3}$ in the same length range. This consistent trend over very different temperatures of 100 and 300 K strongly suggests that the length dependence in the range of > 6.5 μm is due to the superdiffusive behavior of 1D phonons, instead of partially ballistic transport.

This intriguing transport is due to excitation of 1D phonons in the ultra-thin nanowires, as shown in Figure 2d with a linear increasing trend for thinner wires in the temperature range of 50-300 K (upper panel) in contrast to the decreasing trend of thicker wire dure to Umklapp scattering (lower panel).

In addition to this important discovery, we have also done other measurements with the microdevices and published two papers [2,3].

References:

[1] L. Yang, Y. Tao, Y. Zhu, M. Akter, K. Wang, Z. Pan, Y. Zhao, Q. Zhang, Y. Xu, R. Chen, T. T. Xu, Y. Chen, Z. Mao, and D. Li, "Observation of Superdiffusive Phonon Transport in Aligned Atomic Chains," Nature Nanotechnology, published online, DOI: 10.1038/s41565-021-00884-6 (2021).

[2] Z. Pan, L. Yang, Y. Tao, Y. Zhu, Y.-Q. Xu, Z. Mao, and D. Li, "Net Negative Contributions of Free Electrons to the Thermal Conductivity of $NbSe_3$ Nanowires," Phys. Chem. Chem. Phys. 22, 21131-21138 (2020).

[3] Y. Zhao, M. L. Fitzgerald, Y. Tao, Z. Pan, G. Sauti, D. Xu, Y.-Q. Xu, and D. Li, "Electrical and Thermal Transport through Silver Nanowires and their Contacts: Effects of Elastic Stiffening," Nano Lett. 20, 7389-7396 (2020).

Superconducting Thin Film Growth, Process Development, Defects Investigation, and Device Fabrication for Radio-Frequency Accelerating Cavities

CNF Project Number: 2779-19

Principal Investigator(s): Matthias Liepe

User(s): Zeming Sun

Affiliation(s): Cornell Laboratory for Accelerator-based Sciences and Education, Cornell University

Primary Source(s) of Research Funding: National Science Foundation under Grant No. PHY-1549132

Contact: mul2@cornell.edu, zs253@cornell.edu

Website: https://physics.cornell.edu/matthias-liepe

Primary CNF Tools Used: Thermal / e-gun evaporation system, Oxford FlexAL atomic layer deposition system, Jelight 144AX UV ozone generator, Arradiance Gemstar-6 atomic layer deposition system, chemical vapor deposition system, Woollam spectroscopic ellipsometer, Zygo optical profilometer, P10 profilometer

Abstract:

Superconducting radio-frequency (SRF) cavities are the essential component for accelerating charged particle beams that have broad applications such as high-energy colliders, high-intensity X-ray sources, high-precision photolithography, and quantum computing. Niobium tin (Nb_3Sn), conventional niobium (Nb) with a processed/designed surface, niobium titanium nitride (NbTiN), and vanadium silicate (V_3Si) are the most promising superconductor candidates for the next-generation SRF cavities. Here, with the capabilities at the Cornell NanoScale Science and Technology Facility (CNF), we mainly focus on SRF thin film growth development, materials characterization together with sample preparation, post-treatment development to improve RF superconducting properties, and SRF device fabrication to fundamentally understand some SRF physics theories.

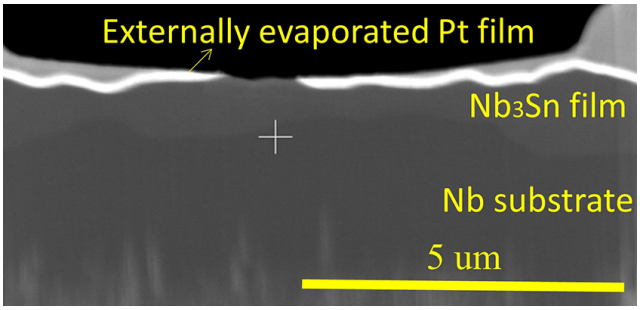

Figure 1: Cross-sectional image of STEM specimens that yield high-resolution atomic imaging.

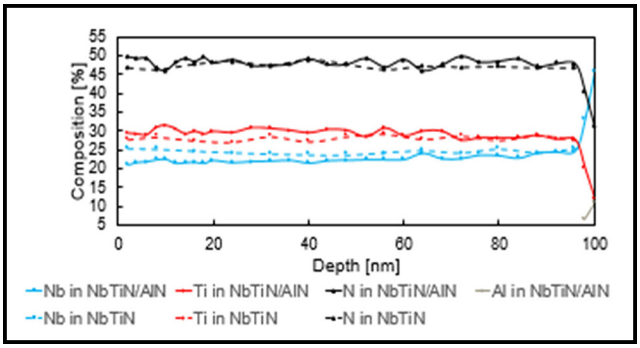

Figure 2: Composition depth profiles of Nb, Ti, N, and Al for atomic-layer-deposited NbTiN/AlN and NbTiN-only films on Nb substrates [5].

Summary of Research:

(1) We demonstrated stoichiometric Nb_3Sn thin films with extremely low surface roughness from electrochemical deposition [1-3]. Reduction of surface roughness and retention of stoichiometry are critical to improving the RF performance of accelerating cavities. We are further investigating the growth mechanism of this Nb_3Sn film using scanning transmission electron microscopy (STEM) through collaborating with Zhaslan Baraissov and Prof. David Muller's research group at Cornell Applied Physics.

High-resolution atomic imaging requires a thin specimen below ~ 10 nm. However, the sample preparation via focused ion beam (FIB) was difficult due to the lack of a proper protection layer for the film surface. We have resolved this issue by depositing an external Pt layer using the e-beam evaporator at CNF (Figure 1), and achieved high-resolution composition and strain mappings [4].

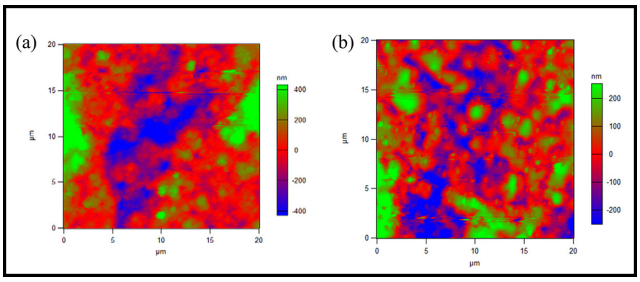

Figure 3: Atomic force microscopy images of Nb_3Sn (a) before and (b) after laser annealing [8].

(2) Alternative deposition approaches such as sputtering, chemical vapor deposition, and atomic layer deposition are being explored to deposit Nb_3Sn, NbTiN, and V_3Si films [2,5-7]. We observed a composition gradient in the atomic-layer-deposited NbTiN films in presence of an hcp-structured aluminum nitride (AlN) layer for the superconductor-insulator-superconductor (SIS) structures (Figure 2) [5]. Moreover, thermal annealing of the sputtered Nb_3Sn and V_3Si films has been systematically investigated on Nb and Cu substrates [6]. In addition, the chemical-vapor-deposition system and process are being developed [7].

(3) Post processes such as ozone treatment, laser annealing, and electropolishing are explored to improve the superconducting film quality. We demonstrated that laser annealing is viable to remove the sharp features on the Nb_3Sn film surface that is coated with a laser absorption layer via an Arradiance Gemstar-6 atomic layer deposition system at CNF (Figure 3) [8]. Also, we successfully electropolished the chemical-vapor-deposited Nb film and reduced the surface roughness by half [9]. Furthermore, we are exploring the Nb surface modification using the Jelight 144AX UV ozone generator at CNF [10].

(4) SRF devices are fabricated using the e-beam evaporator and Oxford FlexAL atomic layer deposition system at CNF, and these devices are being tested to fundamentally understand some SRF theories prior to application of these theories on the large, complex-shaped SRF cavities.

References:

[1] Z. Sun, et al., "Toward stoichiometric and low-surface-roughness Nb_3Sn thin films via direct electrochemical deposition", presented at the International Conference on RF Superconductivity (SRF'21), virtual, June 2021.

[2] Z. Sun, et al., "Study of alternative materials for next generation SRF cavities at Cornell University", presented at the 9th International Workshop on Thin Films and New Ideas for Pushing the Limits of RF Superconductivity, virtual, March 2021.

[3] Z. Sun, et al., "Electrochemical deposition for generating Nb_3Sn films with low surface roughness and stoichiometry", presented at the International Workshop on Nb_3Sn SRF Science, Technology, and Applications (Nb_3SnSRF'20), November 2020.

[4] Z. Baraissov, et al., "Measuring composition variation and lattice strain in Nb_3Sn films", presented at the International Conference on RF Superconductivity (SRF'21), virtual, June 2021.

[5] Z. Sun, et al., "Characterization of atomic-layer-deposited NbTiN and NbTiN/AlN films for SIS multilayer structures", presented at the International Conference on RF Superconductivity (SRF'21), virtual, June 2021.

[6] K. Howard, et al., "Thermal annealing of sputtered Nb_3Sn and V_3Si thin films for superconducting RF cavities", presented at the International Conference on RF Superconductivity (SRF'21), virtual, June 2021.

[7] G. Gaitan, et al., "Development of a system for coating SRF cavities using remote plasma chemical vapor deposition", presented at the International Conference on RF Superconductivity (SRF'21), virtual, June 2021.

[8] Z. Sun, et al., "Surface roughness reduction of Nb_3Sn thin films via laser annealing for superconducting radio-frequency cavities", presented at the International Particle Accelerator Conference (SRF'21), virtual, June 2021.

[9] Z. Sun, et al., "CVD thick Nb film and cavity coating", TESLA Tech. Collaboration workshop, Geneva, Switzerland, Feb, 2020.

[10] Z. Sun, et al., "Surface oxides on Nb and Nb_3Sn surfaces: toward a deeper understanding", presented at the International Conference on RF Superconductivity (SRF'21), virtual, June 2021.